Scientific Papers of
the Department of Electrical Power Engineering of
the Wrocław University of Science and Technology

PRESENT PROBLEMS OF POWER SYSTEM CONTROL

8

Wrocław 2017

Cover design
Piotr PIERZ

Printed in the camera ready form

Department of Electrical Power Engineering
Wrocław University of Science and Technology
Wybrzeże Wyspiańskiego 27, 50-370 Wrocław, Poland
phone: +48 71 320 35 41
www: http://www.weny.pwr.edu.pl/instytuty,52.dhtml; http://www.psc.pwr.edu.pl
e-mail: wydz.elektryczny@pwr.edu.pl

OFICYNA WYDAWNICZA POLITECHNIKI WROCŁAWSKIEJ
Wybrzeże Wyspiańskiego 27, 50-370 Wrocław
http://www.oficyna.pwr.edu.pl
e-mail: oficwyd@pwr.edu.pl
zamawianie.ksiazek@pwr.edu.pl

ISSN 2084-2201

Print and binding: beta-druk, www.betadruk.pl

CONTENTS

synchrophasor estimation, dynamic phasor,
Fourier transform, Taylor–Fourier series,
phase-locked-loop, dynamic filter,

Mirosław ŁUKOWICZ*
Szymon CYGAN*

ANALYSIS OF SYNCHROPHASOR ESTIMATION ERRORS

This papers discusses the analytical analysis of the synchrophasor estimation employed in electrical systems. Short time Fourier transform with the phase locked loop and Taylor Fourier series are analyzed for signals relating to different states which may occur in real power systems. The object is the accurate phasor estimation regardless of the shape of input signal, what for some signal types is cumbersome.

As a result of active and reactive power disturbance in a power system, the frequency deviation and amplitude fluctuations may appear in power system signals. As a consequences of short circuits or overvoltages signal changes occur. This leads to unacceptable errors in short time Fourier transform resulting from Fourier transform properties. This paper presents character of occurring errors and their consequences individually for any signal deviation.

1. INTRODUCTION

An accurate estimation of electrical signal parameters is a vital issue in power system control and protection. Unbalance between the power supply and the load can lead to dynamic changes of the system state, thus voltage and current magnitudes, wave shapes as well as the actual system frequency can vary from nominal values. The efficient control of an electrical network requires more and more accurate information about signal parameters. This include the accurate measure of the phase, the magnitude, the frequency, higher harmonics, Rate of Change of Frequency (ROCOF) and the magnitude change rate. These parameters can be represented in the concise form as a complex valued function referred to as a phasor.

* Wrocław University of Science and Technology, Department of Electrical Power Engineering, Wybrzeże Wyspiańskiego 27, 50-370 Wrocław, Poland, e-mail: miroslaw.lukowicz@pwr.edu.pl, szymon.cygan@pwr.edu.pl

According to synchrophasor standard C37.118.2011 [1], two base classes of estimating algorithms have been defined: P (protection) and M (measurement) class. Both classes are diversified by purpose of application, i.e. P class is designed for cooperation with power system relays. These algorithms are designed to give quick responds to changes in the input signal and to damp response overshoots. M class algorithms are designed for accurate phasor estimation for all signals mentioned in the synhrophasor standard. Requirements for the response time and the acceptable overshoot are milder.

Phasor estimation problem is a well studied issue. The fundamental technique of phasor estimation is based on Short Time Fourier Transform (STFT) of an input signal. STFT is an efficient and a potent way for phasor estimation as long as the frequency of a measured signal does not differ from nominal 50 Hz and a signal amplitude is constant. Occurrence of minor frequency changes yields to disturbance of the algorithm response with the second harmonic and unacceptable estimation errors. The amplitude of the second harmonic is proportional to the difference Δf between the nominal frequency 50 Hz and the actual frequency of the processed signal. The influence of second harmonic distortion can be damped by using a well designed filter or extending integration time in STFT. However, extension of the integration time leads to delay of reporting, and the use of additional filters makes the dynamic more complex. Many different techniques have been used for the proper design of STFT dedicated filters. One approach is based on the expected filter characteristic [2], [3]. This technique allows for adjusting filter properties according to requirements yet does not allow reduction of errors for all expected conditions. The main advantage of windowed STFT algorithms is a low computation cost and an easy implementation.

The vulnerability to frequency variations can be reduced by applying multilevel STFT algorithms [4], as well as algorithms with adaptive filters [5]. In this method the frequency estimate from the previous step is used for the following phasor estimation using the new basis function. This approach increases the algorithm complexity and the numerical burden, but allows obtaining similar estimation errors for full frequency spectrum as for 50 Hz.

The approach based on Taylor phasor approximation has been studied in [6]–[8]. Evaluating of phasor using Least Squares Method (LSM) and approximating of phasor with a polynomial reduce errors caused by the frequency distortion and the amplitude fluctuation, however estimation errors still increase when the frequency distortion rises. This problem can be damped by using the dynamically changing base function in Taylor series based on the previous phasor analysis [9] or the initial STFT evaluation [10]. However, this solution radically increases computational complexity. The crucial issue for Taylor method is the proper adjustment of the polynomial approximation order of Taylor series. The increase of the polynomial order improves the approximation precision and thereby the algorithm accuracy. However, it greatly increases computational burden, requires special approaches to ensure numerical calculation, and leads to the vulnerability to the signal noises. The vulnerability to noises is caused by improved capability to approximate noised function with polynomials of higher orders.

2. PHASOR ANALYSIS

The dynamic phasor has been introduced in [1] as a concept for representation of a complex input signal. Expressing a fast varying real signal as a slow varying complex signal facilitates an analysis. The dynamic phasor is defined for special set of functions such as

$$x(t) = X_m(t)\cos\left(2\pi\int f(t)\mathrm{d}t + \varphi\right) \tag{1}$$

where X_m denotes a varying amplitude of the input signal, φ stands for a constant phase shift, $f(t)$ designates a real time varying frequency of the signal, f_0 is equal to fundamental frequency $\omega = 2\pi f_0$. For each function (1) the dynamic phasor is formulated as

$$X(t) = X_m(t)e^{2\pi i\int (f(t)-f_0)\mathrm{d}t + i\varphi} \tag{2}$$

It can be easily seen that for each real valued signal, the corresponding phasor fulfills following condition. The fundamental component of the input signal is the real part of the rotating phasor

$$x(t) = \mathrm{Re}(X(t)e^{i\omega t}) \tag{3}$$

therefore the phasor is formulated as

$$X(t) = X_m(t)e^{i\psi(t)}) \tag{4}$$

where $\psi(t)$ is a real valued function which denotes the total instantaneous phase shift.

The definition of the dynamic phasor is correct yet incomplete. Therefore, the extra assumption regarding the frequency has to be made to provide the more precise definition. The notation of function in (2) is not unique. Using trigonometric identities the base sinusoidal signal can be expressed with many significantly different forms. Let us consider the sample sinusoidal signal with the nominal frequency 50 Hz, and constant both the amplitude and the phase shift as follows:

$$x(t) = \sin(\omega t) \tag{5}$$

Corresponding to [1] model phasor defined for model signal is of the form (6). Using sample mathematical operations forms (7) and (8) can also be obtained as phasors fulfilling required criteria.

$$x(t)=\cos\left(\omega t-\frac{\pi}{2}\right) \qquad \begin{aligned} X_m(t)&=1 \\ e^{i\psi(t)}&=e^{-i\frac{\pi}{2}}=-i \end{aligned} \tag{6}$$

$$x(t)=2\sin\left(-\frac{\omega t}{2}\right)\cos\left(\frac{\omega t}{2}\right) \qquad \begin{aligned} X_m(t)&=2\sin\left(\frac{\omega t}{2}\right) \\ e^{i\psi(t)}&=e^{-i\frac{\omega t}{2}} \end{aligned} \tag{7}$$

$$x(t)=2\sin\left(\frac{\pi}{2}-\frac{\omega t}{2}\right)\cos\left(\frac{\omega t}{2}-\frac{\pi}{2}\right) \qquad \begin{aligned} X_m(t)&=2\sin\left(\frac{\pi}{2}-\frac{\omega t}{2}\right) \\ e^{i\psi(t)}&=e^{-\left(\frac{\omega t}{2}+\frac{\pi}{2}\right)} \end{aligned} \tag{8}$$

In fact, infinitely many different forms can express the sinusoidal signal just by using trigonometric formulas. This inaccuracy is crucial problem for complete and accurate phasor estimation as far as any input signal is concerned. The most important issue in the phasor estimation is to define the phasor in such a way to get the unique formula for any real valued function.

In C37.118.2011 the phasor uniqueness has been guaranteed by restricting possible forms of the amplitude and the phase shift concerned as time functions, and dividing model functions into the steady state and dynamic functions. The model of the phasor for a steady state is defined as follows

$$\begin{aligned} x(t)&=X_m\cos(\omega_0 t+\varphi)+X_m^k\cos(k\omega_0 t+\varphi_k) \\ X(t)&=X_m e^{i\omega_0 t+\varphi} \end{aligned} \tag{9}$$

The phasor amplitude X_m is any positive constant whereas the phasor phase shift φ is a constant from the range $[0, 2\pi)$. The phasor angular speed ω_0 is constant and it does not differ from nominal frequency more than fixed value that depends on the algorithm type. The harmonic distortion is described by harmonic amplitude X_m^k, which also depends on the algorithm employed. The phasor models for the dynamic states have been defined as follows

$$\begin{aligned} X_m(t)&=X_m(1+at) \\ X_m(t)&=X_m(1+a\chi_{(0,\infty]}(t)) \\ X_m(t)&=X_m(1+a\times\cos(\omega_1 t)) \end{aligned} \tag{10}$$

where $X_m(t)$ is a polynomial of order 1, or the step function, or the cosine wave. The phase shift variability can be characterized with the polynomial of order 2, the step function, or cosine function as follows

$$\begin{aligned} \psi(t) &= \psi_0(1 + a_1 t + a_2 t^2) \\ \psi(t) &= \psi_0(1 + a\chi_{(0,\infty]}(t)) \\ \psi(t) &= \psi_0(1 + a \times \cos(\omega_1 t)) \end{aligned} \tag{11}$$

The aforementioned definition under appropriate assumptions for a and ω_1 coefficients provides unique representation for each function from standard test class, but does not cover all periodic functions. There exist reasonable periodic functions which phasors do not belong to the standard class.

Another problem coming with the phasor definition is a constricted reversibility. Let us assume that there are two periodic real valued signals formulated as follows

$$\begin{aligned} x_1(t) &= X_{m_1}(t)\,\mathrm{Re}(e^{i\omega t} e^{i\varphi_1(t)}) \\ x_2(t) &= X_{m_2}(t)\,\mathrm{Re}(e^{i\omega t} e^{i\varphi_2(t)}) \end{aligned} \tag{12}$$

which are close to each other in L^2 norm and RMS of their difference is close to zero. The small RMS of the function difference does not imply small amplitude and phase differences. Though functions $x_1(t)$ and $x_2(t)$ are almost equal, their phasors can be significantly different. Therefore, restricted function values lead to the numerically ineffective reversibility.

3. PHASOR ESTIMATION

3.1. PROBLEM DEFINITION

The phasor estimation is a process of finding the corresponding phasor for input signal, based on finite number of probes. For any input signal $x(t)$ it is necessary to find the amplitude $X_m(t)$ and the phase shift $\varphi(t)$ which are close to values of the model. Every phasor estimation algorithm has three main parameters, which describe algorithm efficiency, namely: the Total Vector Error (*TVE*), the Frequency Error (*FE*) and the Rate of Change of Frequency Error (*RFE*). *TVE* is defined as the relative difference between estimated phasor $\hat{X}(t)$ and model phasor $X(t)$. *TVE* is an indicator characterizing absolute difference between estimated and real phase shift as well as between estimated and real amplitude.

$$TVE = \frac{\left|\hat{X}(t) - X(t)\right|}{\left|X(t)\right|} \tag{13}$$

FE is defined as a relative difference between the model frequency and its estimated value.

$$FE = \frac{\left|\hat{f} - f_{\mathrm{real}}\right|}{\left|f_{\mathrm{real}}\right|} \tag{14}$$

RFE is defined in the analogous way as

$$RFE = \frac{\left|d\hat{f} - \frac{df_{\mathrm{real}}}{dt}\right|}{\left|\frac{df_{\mathrm{real}}}{dt}\right|} \tag{15}$$

Indices *TVE*, *FE*, *RFE* can be roughly interpreted as relative differences between zero, first and second derivative of the complex valued function. The main goal for each estimation algorithm is to keep *TVE*, *FE* and *RFE* as small as possible for all functions in the model function set.

3.2. TEST SIGNAL

Algorithms presented in this paper have been analyzed for signals presented in the model class set. All tests have been performed for boundary signals in the model set class to exhibit estimation problems occurring for these signals. The test signal is presented in Fig. 1, in the form of the model phasor. The signal is composed of 34 different model signals of the critical behavior. Model signals are numbered on x axis. The first diagram shows input signal frequency, the second and third ones show the real and imaginary parts of the model phasor. The model signal has been arranged as follows:

- 1 sinusoidal 50 Hz wave with amplitude of 1,
- 2, 3 sinusoidal 48 Hz and 52 Hz waves with amplitude of 1,
- 4–9 sinusoidal 50 Hz waves with ramp of amplitude,
- 10–15 sinusoidal waves with ramp of frequency,
- 16–20 sinusoidal waves distorted with higher harmonics
- 21–24 sinusoidal waves with step changes of amplitude
- 25–28 phase step changes,
- 29 phase oscillation,
- 30 amplitude oscillation,
- 31–34 sinusoidal waves of frequency 45, 50, 55 Hz and amplitude 1.

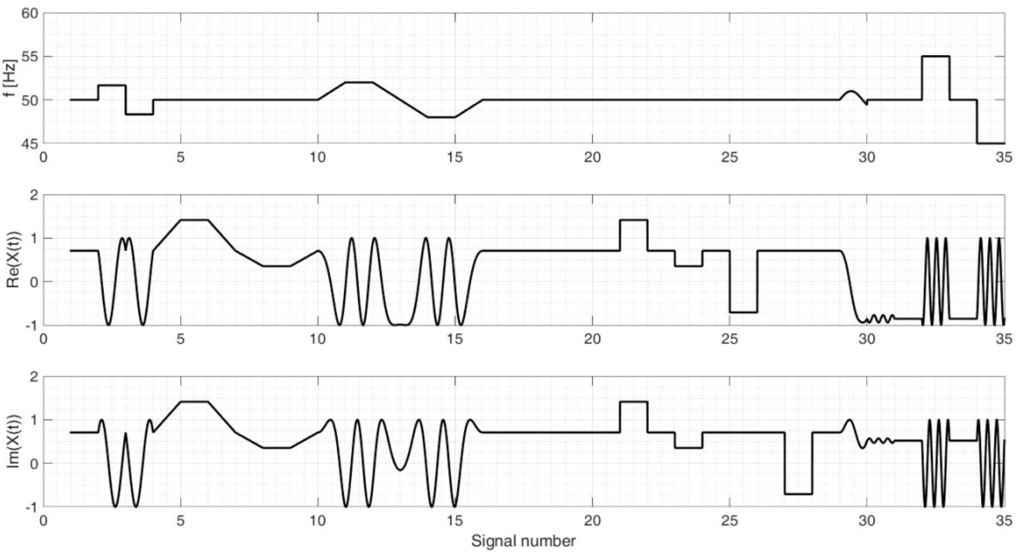

Fig. 1. Frequency, real part and imaginary part of testing phasor

4. FOURIER TRANSFORM BASED ALGORITHM

4.1. FOURIER ANALYSIS

Let us consider the set of test functions (1). According to Fourier series theory, each periodic sufficiently smooth function $x(t)$ with the angular speed ω can be represented as Fourier series formulated as follows

$$x(t) = \sum_{k=-\infty}^{\infty} a_k e^{i\omega kt} \tag{16}$$

Fourier coefficients are obtained from

$$a_k = \int_D x(t) e^{i\omega kt} \tag{17}$$

where D denotes a window length. Typically, D is equal to the integer number of periods.

For functions with constant, amplitude, phase and the nominal frequency of 50 Hz, normalized phasor can be expressed as first term in Fourier series a_1, or its conjugation a_{-1}. The fundamental idea for STFT is to extend phasor estimation as a_1 coefficient for each function in the model function set. Unfortunately, applying Eq. (17) to functions with varying amplitude or varying phase shift yields to high errors of phasor estimation. Functions with an amplitude and a phase time dependent are no longer periodic with frequency of 50 Hz in mathematical sense. Evaluated STFT for such signal is distorted by higher harmonics. Harmonic distortion rate is proportional to the amplitude and phase shift variability.

Fourier series algorithm can by significantly improved by modifying the window function. The application of additional filters reduces the influence of higher harmonic distortions. Formulas for the approximated phasor are as follows

$$y(t) = \int_{t-\frac{nT}{2}}^{t+\frac{nT}{2}} x(\tau) e^{i\omega\tau} g(t-\tau) \mathrm{d}\tau \tag{18}$$

where window function $g(t)$ determines the algorithm efficiency and also its static and dynamic characteristics.

In pure STFT the window function $g(t)$ is continuously equal to $1/D$, which implies the gain less or equal to one. In C37.118 [1] two base filters have been proposed for P and M class algorithms. Studying proper filter design is not a topic of this paper. For further investigations the window filter will be selected as the 2 periods triangle function of the form

$$g_T = \begin{cases} \left|1 - \dfrac{t}{T}\right|, & |t| \le T \\ 0, & |t| > T \end{cases} \tag{19}$$

where filter window $g_T(t)$ is designed to neutralize disturbances during linear amplitude changes. Furthermore, filter with $g_T(t)$ window function ensures perfect damping of higher harmonics distortion in input signal.

In real systems STFT is performed for finite number of probes. Integrals in expressions (17), (18), are substituted with finite sums. Fourier coefficients are calculated with following formula

$$a_k = \sum_{l=-\frac{N}{2}}^{\frac{N}{2}} x(l) e^{i\omega \frac{k}{f_p} t} \tag{20}$$

where f_p is sampling frequency. N is selected with respect to ω to keep integer values of $\dfrac{2\pi f_p}{\omega N}$. For algorithms with a window function the phasor is evaluated analogously from

$$y(m) = \sum_{l=m-\frac{N}{2}}^{m\frac{N}{2}} x(l) e^{i\omega\frac{k}{f_p}t} g_{\frac{N}{2}}(l-m) \tag{21}$$

The crucial issue for substituting integrals with finite sums is preserving base properties of STFT. Simply, Fourier coefficients are constant for base frequency signals of time independent amplitude and phase.

4.2. SIMULATION OUTCOMES

Results for TVE obtained on test signal are presented in Fig. 2. It can be observed that for signals of 50 Hz frequency and the constant amplitude (signals 1, 4–10, 16–28, 31 33), phasor estimation errors are almost negligible on the level of 10^{-7} p.u. Proper window design allows bypassing estimation errors for linear ramp of amplitude (signals 4–10). Crucial errors occurs for signals with frequencies other than 50 Hz (2, 3, 11, 14, 32, 34), for ramp of frequency (10, 12, 13, 15), frequency (29) and amplitude (30) fluctuations. Errors occurring due to frequency deviation have two primal components. First of all, the deviation from the base frequency increases the amount of higher harmonics in output signal as a consequence of window length mismatch. Secondly, the filter gain and the filter phase shift is not constant as is not a frequency function in the neighborhood of the base frequency. The additional compensating function which reacts against filter characteristic is required to mitigate these errors.

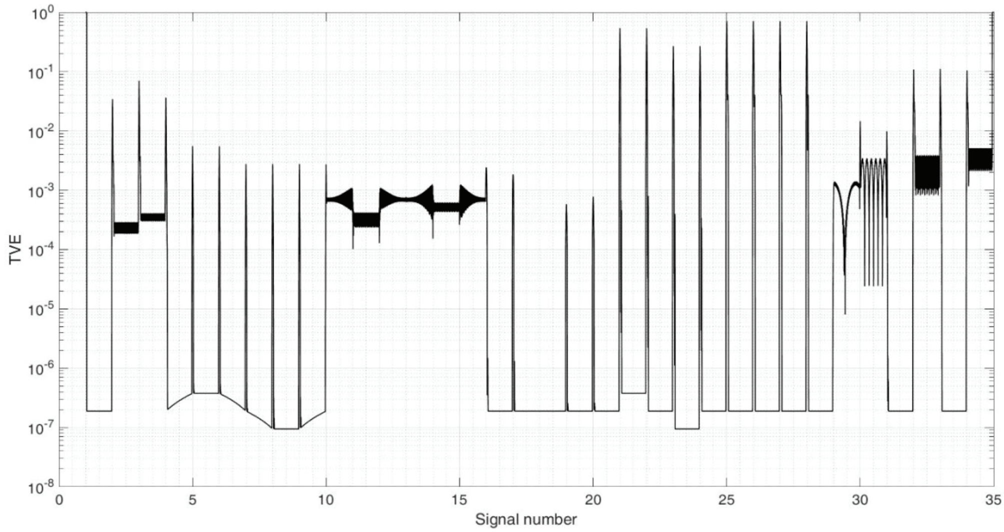

Fig. 2. Simulation results for STFT algorithm with triangle window

5. FOURIER TRANSFORM WITH PHASE LOCKED LOOP

5.1. CONTINOUS ANALYSIS

For static signals which frequencies differ from the base frequency, TVE increases rapidly when $|\Delta f|$ goes up. The primary issue for phase locked up algorithms is to reduce errors occurring due to frequency disturbance by modifying the base frequency in Fourier algorithm. STFT with the modified frequency used for phasor estimation reduces the amount of higher harmonics without disrupting orthogonality relation. The schema of the algorithm is shown in Fig. 3.

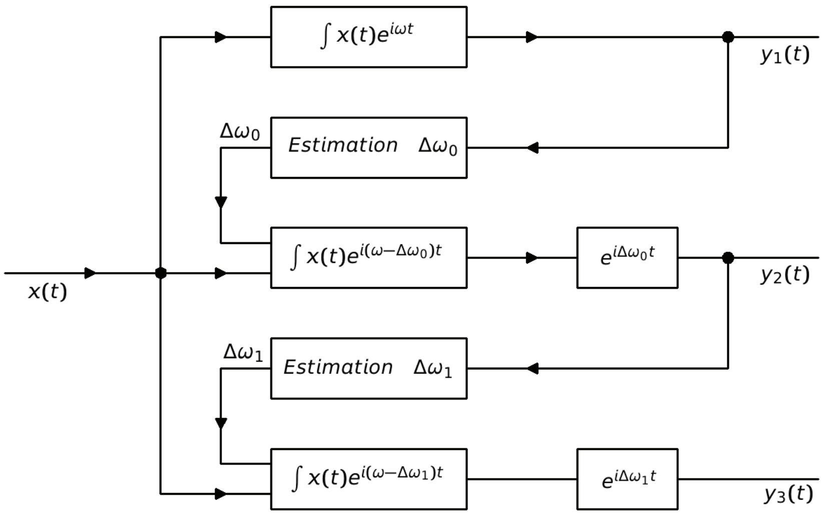

Fig. 3. Scheme of phase locked loop algorithm

For input signal $x(t)$, first phasor approximation $y_1(t)$ is evaluated using STFT.

$$y_1(t) = \int_{t-\frac{N}{2}T}^{t+\frac{N}{2}T} x(\tau)e^{i\omega\tau} g_{\frac{N}{2}T}(\tau - t)\,\mathrm{d}\tau \tag{22}$$

On the base of $y_1(t)$ the frequency difference between real and normalized frequency can be evaluated by using the frequency estimation algorithm. This yields to first angular speed approximation $\omega - \Delta\omega_0$. As noted above, the error rate depends on the frequency disturbance, so evaluating STFT in base angular $\omega - \Delta\omega_0$ reduces errors caused by the frequency discrepancy. Evaluating STFT in new basis requires window modification. The integration period needs to match a new angular speed. The new phasor in base $\omega - \Delta\omega_0$ is evaluated with the following formula

$$y_2(t) = \int_{t-\frac{N}{2}T_1}^{t+\frac{N}{2}T_1} x(\tau)e^{i(\omega-\Delta\omega_0)\tau} g_{\frac{N}{2}T_1}(\tau - t)\mathrm{d}\tau \tag{23}$$

where

$$T_1 = \frac{1}{f - \Delta f_0} = \frac{2\pi}{\omega - \Delta\omega_0} \tag{24}$$

The phasor evaluated with STFT of modified frequency is expressed in the base of the periodic function with angular speed $\omega - \Delta\omega_0$. The normalized phasor is defined in the base of the periodic function with angular speed ω. The adjustment is obtained by rotating the second level estimation with difference frequency $\Delta\omega_0$. Phasor $y_2(t)$ obtained with this method can be used to iteratively evaluate the new frequency difference and STFT in $\omega - \Delta\omega_1$ basis. Phasor $y_3(t)$ is then calculated from

$$y_3(t) = \int_{t-\frac{N}{2}T_2}^{t+\frac{N}{2}T_2} x(\tau)e^{i(\omega-\Delta\omega_1)\tau} g_{\frac{N}{2}T_2}(\tau - t)\mathrm{d}\tau \tag{25}$$

where

$$T_1 = \frac{1}{f - \Delta f_1} = \frac{2\pi}{\omega - \Delta\omega_1} \tag{26}$$

In the mathematical model, where Fourier coefficients are obtained by integrating, the sequence of iterated phasors converges to the model phasor.

5.2. DISCRETE ANALYSIS

Applications of the phase locked loop Fourier algorithm to a discrete signal suffers from the crucial problem. Discrete STFT algorithms produce errorless results as long as integration time is uniformly partitioned into probing time. To illustrate this problem let us consider the discrete input signal with the constant amplitude, the phase shift equal to 0, and with angular speed ω' which may differ from base angular speed ω. The proper phasor approximation is expected to be obtained, if angular speed ω' is known. It is necessary to know proper window length N to apply STFT with ω', however the calculated window length may not match probing frequency, what means $\frac{2\pi f_p}{\omega' N}$ isn't integer. This problem is illustrated in Fig. 4.

It follows that obtained Fourier coefficients are modified by mismatch error $f_k(E)$ which strongly depends on the reciprocal relation between ω and ω'.

$$a_k(m) = \sum_{l=m-\frac{N}{2}}^{m+\frac{N}{2}} x(l) e^{ik\omega' \frac{l}{f_p}} g_{\frac{N}{2}}(l-m) + f_k(E)(m) \tag{27}$$

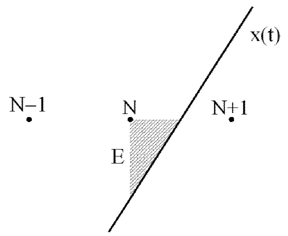

Fig. 4. Mismatch error

The mismatch error is a time varying complex valued function, which depends also on probe number m. The error can be negated by modification of window function g with respect to ω. This can be easy proven for a trivial window function used in pure STFT algorithm, however for other window functions it is much more complicated. Modifications can be performed locally, for single filter coefficient (28), or globally for multiple coefficients (29). The application of global modifications increases computational complexity but reduces vulnerability to external disturbances. It can be shown that for triangle type filter $g_{N/2}$, the mismatch error for the local compensation is expressed by

$$f_k(E)(m) = C(l) x(m-l) e^{ik\omega' \frac{m-l}{f_p}} \tag{28}$$

and for global compensation, with weighted function $D(l)$

$$f_k(E)(m) = \sum_{l=-\frac{N}{2}}^{\frac{N}{2}} C(l) x(m-l) e^{ik\omega' \frac{m-l}{f_p}} D(l) \tag{29}$$

where, $-\frac{N}{2} \le l \le \frac{N}{2}$, $C(l)$ is a complex function of l.

New filter window $g'_{N/2}$ can be obtained by modification of each l-th coefficient with weighted function $C(l)$ and the normalization process to keep the amplification less or equal to one.

Results presented in this section have been obtained for the single modification of middle filter value $C(0)$. Function $C(0)(\omega')$ is still dependent on frequency discrepancy ω'. Function $C(0)(\omega')$ graph is presented in Fig. 5. When the frequency is equal to 50 Hz, the matching condition is fulfilled and no additional compensation is necessary, i.e. compensation is equal to 0. The deviation from the base frequency increases the mismatch error, and hence the degree of compensation. Function C is asymmetric about 50 Hz. This is so because the area of the mismatch field is a nonlinear frequency function.

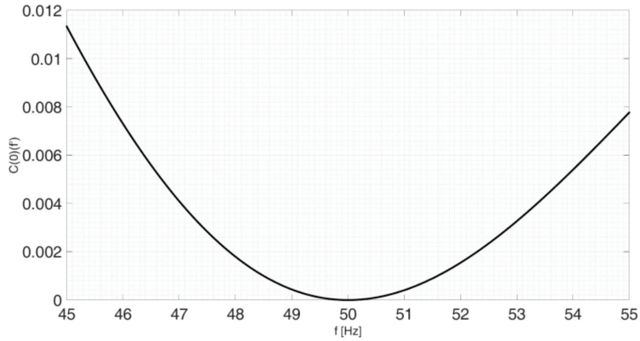

Fig. 5. Modification function for middle filter coefficient $C(0)$

5.3. SIMULATION RESULTS

Results obtained for Fourier phase locked loop algorithm are presented in Fig. 6. TVE for three levels of STFT is submitted – blue line is for pure STFT algorithm, red

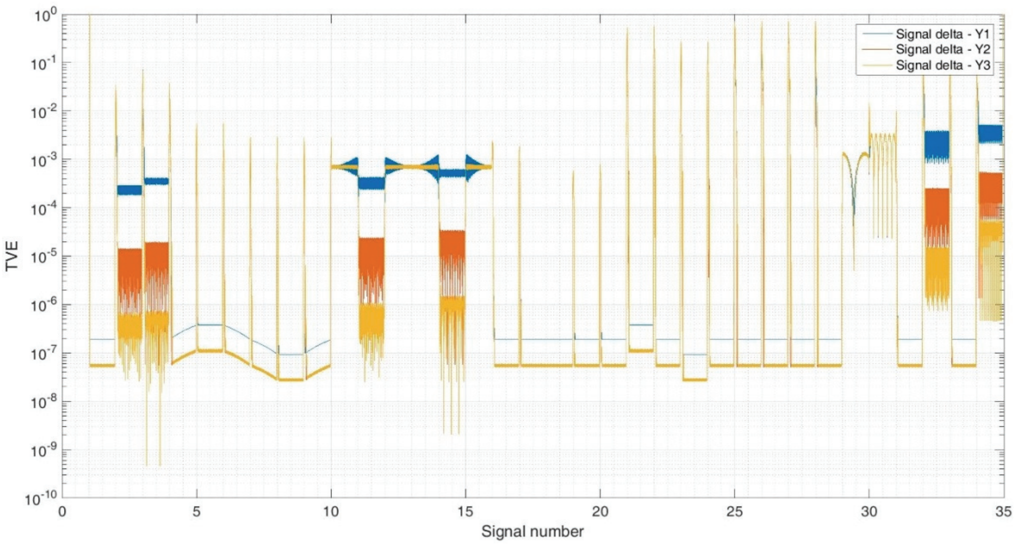

Fig. 6. Simulation results for phase locked loop STFT with triangle window

corresponds to STFT with one loop and yellow denotes a double loop. It can be observed that for signals with frequency equal to 50 Hz and constant amplitude phasors, TVE for all estimators is negligible. Minor differences between TVEs are followed by the inaccuracy in filter compensation function. Major improvement was obtained for signals with the constant frequencies differing from 50 Hz (2, 3, 11, 14, 32, 34). The first estimation (Y_1) of the phasor is burdened with heavy errors. On the basis of Y_1, the first frequency approximation was evaluated, which was closer to real vale than base 50 Hz. This approach improves the second estimation (Y_2) which is about 10 times more precise than previous one. Evaluating third approach (Y_3) allows achieving the accuracy that is comparable with the accuracy for a signal with the base frequency of 50 Hz. The further iterating lock loop process is groundless, because frequency mismatch errors are dominated by errors deriving from the magnitude and phase compensation inaccuracy. Estimation errors are preserved on the negligible level for signals with harmonic distortion (16-20), caused by retaining the orthogonality relation in multilevel STFT algorithm.

It can be observed that for signals with ramp of frequency (11, 12, 13, 15) as well as for the frequency (29) and amplitude fluctuation (30), iterative phasor evaluation does not efficiently improve the algorithm accuracy. For ramp of frequency, TVE is kept on the level corresponding to ramps around 50 Hz for the full frequency spectrum. For signals with parameter fluctuations all three phasors show the same error level. This is because estimated signals are fluctuating near the frequency of 50 Hz.

6. TAYLOR FOURIER SERIES ALGORITHM

6.1. TAYLOR SERIES EXPANSION

Taylor series expansion has been introduced to improve phasor estimation for amplitude and phasor estimation. Let us consider a function $x(t)$ with corresponding phasor $X(t)$. By phasor definition the following equation holds

$$x(t) = \mathrm{Re}(X(t)e^{i\omega t}) = \frac{X(t)e^{i\omega t} + \overline{X(t)e^{i\omega t}}}{2} \tag{30}$$

where $\overline{X(t)}$ denotes conjugation. According to Weierstrass approximation theorem, phasor $X(T)$ can be approximated with N – order complex polynomial as follows

$$X(T) \approx \sum_{k=0}^{N} a_k t^k = \mathbf{AT} = \sum_{k=0}^{N} b_k p_k(t) = \mathbf{BP}(t)$$

$$\mathbf{A} = (a_0 \quad a_1 \quad \ldots \quad a_{N-1} \quad a_N)$$

$$\mathbf{B} = (b_0 \quad b_1 \quad \ldots \quad b_{N-1} \quad b_N) \tag{31}$$

$$\mathbf{T} = (1 \quad t \quad \ldots \quad t^{N-1} \quad t^N)$$

$$\mathbf{P}(t) = (p_0(t) \quad p_1(t) \quad \ldots \quad p_{N-1}(t) \quad p_N(t))$$

where coefficients a_k are complex numbers. By choosing the set of polynomials $p_k(t)$, (31) can be expressed as a sum of polynomials, where $p_k(t)$ is a polynomial of order k. The problem can be formulated as

$$x(t) \approx \frac{\mathbf{BP}e^{i\omega t} + \overline{\mathbf{B}}\mathbf{P}e^{-i\omega t}}{2} = \frac{1}{2}(\mathbf{B} \quad \overline{\mathbf{B}})\begin{pmatrix} \mathbf{P}(t)e^{i\omega t} \\ \mathbf{P}(t)e^{-i\omega t} \end{pmatrix} \tag{32}$$

Multiplying both sides of (32) by transposition of $\begin{pmatrix} \mathbf{P}(t)e^{i\omega t} \\ \mathbf{P}(t)e^{-i\omega t} \end{pmatrix}$ we obtain

$$x(t)(\mathbf{P}'(t)e^{i\omega t} \quad \mathbf{P}'e^{-i\omega t}) \approx \frac{1}{2}(\mathbf{B} \quad \overline{\mathbf{B}})\begin{pmatrix} \mathbf{P}(t)\mathbf{P}'(t)e^{i2\omega t} & \mathbf{P}(t)\mathbf{P}'(t) \\ \mathbf{P}(t)\mathbf{P}'(t) & \mathbf{P}(t)\mathbf{P}'(t)e^{-i2\omega t} \end{pmatrix} \tag{33}$$

In order to obtain the polynomial approximation of the phasor, matrix ($\mathbf{B}$ conj($\mathbf{B}$)) has to be evaluated. The matrix on the right hand side consists complex functions, which columns are linearly dependent. It follows that the matrix is irreversible for any t. To obtain the linear dependence it is sufficient to transform the matrix of functions into the matrix of numbers, and to ensure the linear independence. The integration of both sides of (33) Yields

$$\int x(t)(\mathbf{P}'(t)e^{i\omega t} \quad \mathbf{P}'(t)e^{-i\omega t}) \approx \frac{1}{2}(\mathbf{B} \quad \overline{\mathbf{B}})\int\begin{pmatrix} \mathbf{P}(t)\mathbf{P}'(t)e^{i2\omega t} & \mathbf{P}(t)\mathbf{P}'(t) \\ \mathbf{P}(t)\mathbf{P}'(t) & \mathbf{P}(t)\mathbf{P}'(t)e^{-i2\omega t} \end{pmatrix} \tag{34}$$

The proper set of polynomials P simplifies the expression, giving

$$\int x(t)(\mathbf{P}'(t)e^{i\omega t} \quad \mathbf{P}'e^{-i\omega t}) \approx \frac{1}{2}(\mathbf{B} \quad \overline{\mathbf{B}})\begin{pmatrix} \int \mathbf{P}(t)\mathbf{P}'(t)e^{i2\omega t} & I \\ I & \int \mathbf{P}(t)\mathbf{P}'(t)e^{-i2\omega t} \end{pmatrix} \tag{35}$$

The multiplication of (35) by the inverse matrix gives

$$\frac{1}{2}(\mathbf{B} \quad \overline{\mathbf{B}}) \approx \int x(t)(\mathbf{P}'(t)e^{i\omega t} \quad \mathbf{P}'e^{-i\omega t})\begin{pmatrix} \int \mathbf{P}(t)\mathbf{P}'(t)e^{i2\omega t} & I \\ I & \int \mathbf{P}(t)\mathbf{P}'(t)e^{-i2\omega t} \end{pmatrix} \tag{36}$$

The dynamic phasor estimated integrating time domain is expressed as (31). The immediate phasor value for time $t = 0$ is obtained as b_0, i.e. first element in matrix **B**.

6.2. SIMULATION RESULTS

Results obtained for Fourier Taylor series algorithm are depicted in Fig. 7. Analysis has been performed for polynomials of order 2 (blue), 4 (red) and 6 (yellow). It can be observed that for signals with the base frequency of 50 Hz and without higher harmonic distortion (1, 4–9, 20–28, 31, 33), the best estimation accuracy is achieved for any polynomial order, the same as for STFT algorithms. For signals with frequency disturbances, liner frequency changes, as well as frequency and amplitude fluctuations (2, 3, 10-15, 29, 30, 32, 34), increasing polynomial order improves the estimation efficiency. For the signal with the higher harmonics content (16–19) the occurring error is higher. It follows form both the property of LSM and the non-uniqueness of the phasor. Each signal with higher harmonic distortion can be formulated as a dynamic phasor without higher harmonics but with varying amplitude and/or varying phase shift. This phasor is approximated by a polynomial instead of being damped.

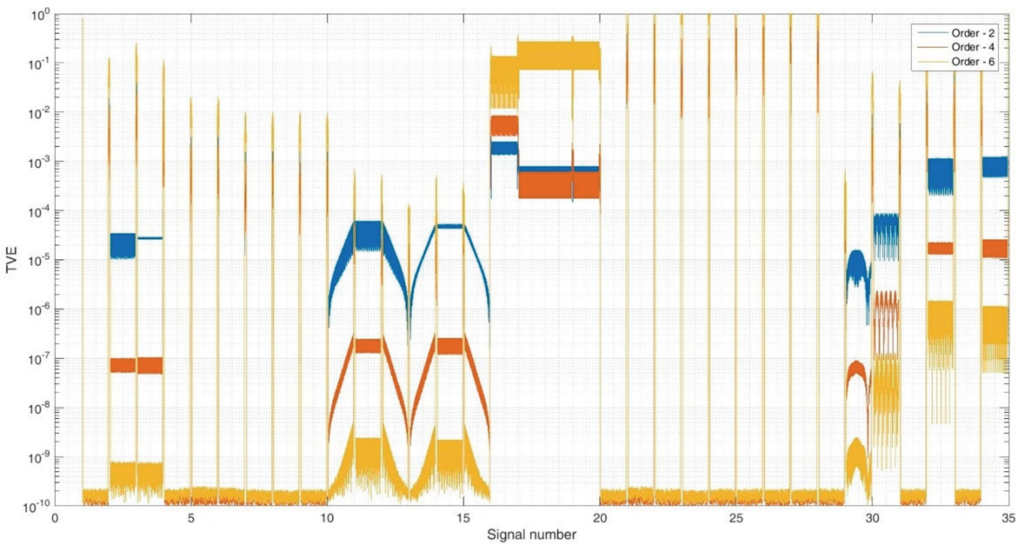

Fig. 7. Simulation results for Taylor-Fourier series method

Therefore, for the pure Taylor series algorithm the orthogonality relation no longer holds. Orthogonality can be ensured by extending the function base with complex functions with higher frequency $P(t)e^{ik\omega t}$, for $k > 1$. The best suiting polynomial form of the approximation is determined by the required algorithm accuracy, the acceptable computational complexity, and the capability of inverse matrix evaluation.

7. CONCLUSION

This work has shown reasons of synchrophasor estimation errors in electrical power systems. STFT and Fourier Taylor series based algorithms were studied to determine their advantages and disadvantages as well as possibilities for further efficiency improvement.

Investigations have revealed that algorithms based on STFT as well as phase locked algorithms are efficient as long as amplitude and frequency of the processed signal are constant. According to previous phasor analysis one signal can have many phasor representations. It follows that the signal with varying amplitude and/or frequency, can be considered as different signals with the harmonic distortion. In consequence, important signal parameters are being expressed as higher harmonics. As higher harmonics are damped by applied filters, some signal information is lost in the phasor representation.

Efficiency of Taylor Fourier series based algorithms strongly depends on the polynomial order adopted for the phasor approximation. Firstly, appropriate selection of the polynomial order is strongly determined by accuracy requirements, restrictions on the response overshoot and the capability of the harmonic distortion damping. Secondly, properties of the integration process in Taylor Fourier method need to be well stated. By modifying the integrating function in LSM, dedicated properties can be acquired. The estimation accuracy can be improved also by substituting polynomial approximation by the nonlinear approximation and by modification of LSM, however further research needs to be conducted.

REFERENCES

[1] IEEE Standard for Synchrophasor Measurements for Power Systems, IEEE Standard C37.118.1-2011, Dec. 2011.

[2] MACII D., BARCHI G., PETRI D., *Design Criteria of Digital Filters for Synchrophasor Estimation*, Instrumentation and Measurement Technology Conference (I2MTC), 2013 IEEE International, Minneapolis, MN, USA, 2013.

[3] ROMANO P., PAOLONE M., *Enhanced Interpolated-DFT for Synchrophasor Estimation in FPGAs: Theory, Implementation, and Validation of a PMU Prototype*, IEEE Transactions on Instrumentation and Measurement, December 2014, Vol. 63, No. 12.

[4] ROSCOE A.J., ABDULHADI I.F., BURT G.M., *P-Class Phasor Measurement Unit Algorithms Using Adaptive Filtering to Enhance Accuracy at OffNominal Frequencies*, IEEE International Conference on Smart Measurements for Future Grids (SMFG), Bologna, Italy, 2011.

[5] ROSCOE A.J., ABDULHADI I.F., BURT G.M., *P and M Class Phasor Measurement Unit Algorithms Using Adaptive Cascaded Filters*, IEEE Transactions on Power Delivery, July 2013, Vol. 28, No. 3.
[6] PLATAS-GARZ M., SERNA J., *Dynamic Phasor and Frequency Estimates through Maximally Flat Differentiators*, IEEE Transactions on Instrumentation and Measurement, July 2010, Vol. 59, No. 7.
[7] MAI R.K., HE Z.Y., FU L., KIRBY B., BO Z.Q., *A Dynamic Synchrophasor Estimation Algorithm for Online Application*, IEEE Transactions on Power Delivery, April 2010, Vol. 25, No. 2.
[8] BELEGA D., FONTANELLI D., PETRI D., *Low-Complexity Least-Squares Dynamic Synchrophasor Estimation Based on the Discrete Fourier Transform*, IEEE Transactions on Instrumentation and Measurement, December 2015, Vol. 64, No. 12.
[9] SERNA J., *Synchrophasor Measurement with Polynomial Phase-Locked-Loop Taylor–Fourier Filters*, IEEE Transactions on Instrumentation and Measurement, February 2015, Vol. 64, No. 2.
[10] FU L., ZHANG J., XIONG S., HE Z., MAI R., *A Modified Dynamic Synchrophasor Estimation Algorithm Considering Frequency Deviation*, IEEE Transactions on Smart Grid, March 2017, Vol. 8, No. 2.

insulation, distribution network,
ground fault, signal injection

Maryna KYRYCHENKO*
Marcin HABRYCH**

SYSTEM OF SIGNAL INJECTION AND EXTRACTION FOR PROTECTION AND INSULATION MONITORING IN MEDIUM VOLTAGE NETWORKS

Simple overcurrent criterion is most often used for detection and elimination of ground faults in radial industrial medium voltage networks. Since in Poland medium voltage networks work with non-effectively grounded neutral point, the ground fault currents can reach very low values, especially under high resistance faults. Such faults cannot be detected by any protection. Therefore, new methods to detect ground faults and to control the insulation in medium voltage network are of great importance. In the paper the idea for monitoring insulation parameters of the system, based on the simultaneous use of two different signals of non-industrial frequency, injected into the controlled network, is presented and discussed.

1. INTRODUCTION

European Union legislation and the actions of electricity market regulators in European countries issue a challenge to subjects in the field of power engineering that are connected with the increase of reliability and continuity of energy supply, energy efficiency increase, etc.

Energy supply continuity is strongly related to the reliability of the medium voltage (MV) distribution networks. Therefore, the increase of the reliability of MV networks is a key problem of any country, particularly due to strong energy dependence of each other.

The most common faults in MV networks are the single-phase faults to the ground (about 60–70%). The main reason for the ground faults appearance is the degradation of cable line insulation due to many factors like overvoltages and environmental hazard.

* State Higher Educational Institution "National Mining University", Ukraine.
** Department of Electrical Power Engineering, Wrocław University of Science and Technology, Wybrzeże Wyspiańskiego 27, 50-370 Wrocław, Poland.

Of course it is impossible to avoid the ground faults completely, but there are some ways to reduce their occurrence to prevent deterioration of insulation and reduce hazard level for people. The continuous monitoring of insulation parameters should be carried out. There are cases of lack of response of power system protection during low-current ground faults. It all makes the need of research for new methods of insulation monitoring and modernization criteria for the protection operation.

Therefore, the development of the system of signal injection and extraction for network protection and insulation monitoring in MV network is an important issue not only scientifically, but also industrially [1–3].

2. GROUND FAULTS IN NON-EFFECTIVELY GROUNDED MEDIUM VOLTAGE NETWORK

When protecting lines and MV equipment against ground faults the most commonly used criterion is simple overcurrent criterion. Signal from the zero-sequence current filter goes to relays, such as Ferranti CT (for cables) or Holmgreen system (for overhead lines). Starting current value I_{0r}, set on protection, must be rebuilt from the capacitive currents of own line and from the error currents of zero-sequence current filters.

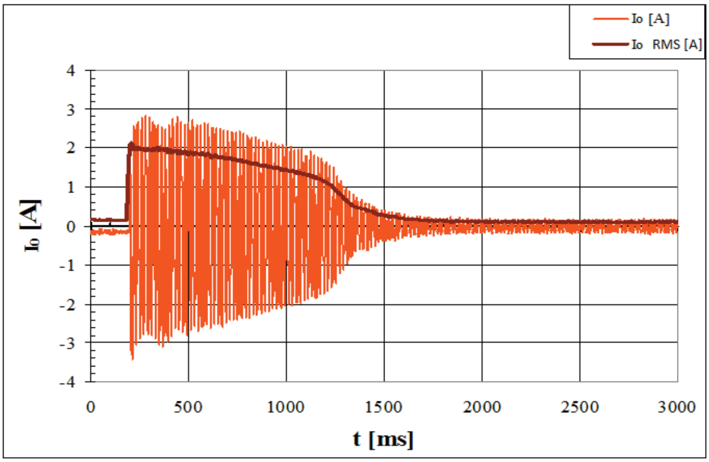

Fig. 1. A signal waveform (error) at the output of current transformer to measure zero sequence current during switching the pump motor of 400 kW power [1]

Figure 1 shows the selected error current waveform of Ferranti CT, registered in the isolated 6 kV network during starting of an asynchronous motor with nominal power of 400 kW driving a pump (without ground fault).

Phase current at the beginning of the motor start was approximately 200 A. Under these conditions the signal appearing at the current transformer output for measurement of the zero sequence current must be interpreted as an error signal.

As it results from the waveform of zero sequence current I_0 shown in Figure 1, an rms value in the initial period of motor start, exceeds 2A and goes to values close to zero after the time above 1.2 seconds. Consequently, when setting up this starting values the above error currents from the Ferranti CT should be taken into account. Such a low value of starting currents may cause a standard protection unable to detect a low-current faults (high-resistance). As an example of this situation might be the fault shown in Fig. 3. In the same power station, a fault was made by placing the cable on the surface of the earth on the one side connected to a selected phase, as shown in Fig. 2.

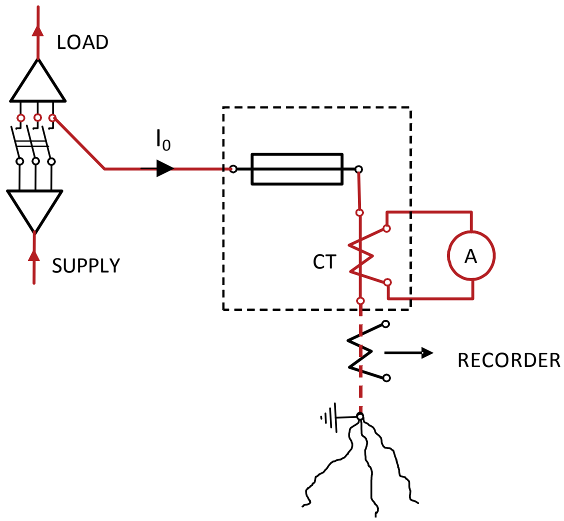

Fig. 2. Scheme of measurement system for a single-phase resistive ground faults

Figure 3 shows the waveform of zero sequence current I_0 as a function of time, where it could be seen an envelope curve of fault current that allows the evaluation of the fault phenomenon waveform. R_{ms} value of the fault current for t = 0 was about 1.5 A and in the steady state does not exceed 0.3 A.

As it results from the shown waveform, the current value in steady state is considerably lower than the starting value setting in protection. This means, that with this setting the protection is not able to detect the resistive ground fault of the line.

According to above mentioned, research is being conducted on various other detection methods of low-current ground faults or deterioration of the cable insulation [1, 4, 5]. One of these methods could be the system injection into MV network of signals with a frequency differing from the rated network frequency.

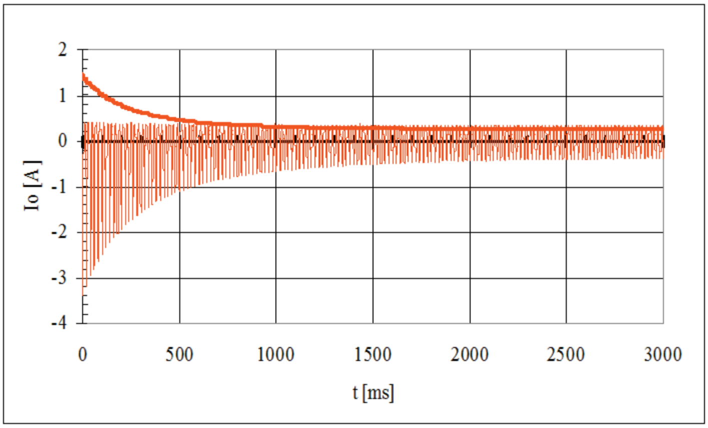

Fig. 3. The waveform of zero sequence current I_0 at the time of resistive ground faults [1]

3. SYSTEM OF CURRENT INJECTION INTO THE MEDIUM VOLTAGE NETWORK

For selective and continuous monitoring of insulation parameters a method based on the simultaneous use of two signals of non-industrial frequency injected into a controlled network was developed. A scheme of such a system is shown in Fig. 4.

Many techniques are known with use of current signals injection both AC and DC. In contradistinction from other methods, a concept of simultaneous use of two signals of non-industrial frequency allows to define separately resistance R and capacity C, not only the impedance Z as in case of one signal injection.

The most optimal construction scheme of any microprocessor system is the design of a modular principle of the system [6].

The microprocessor system, that implements the method of continuous monitoring of insulation components values of distribution network in normal operating conditions consists of the following functional blocks:

- the block of signal injection;
- the block of signal extraction and processing;
- the block of matching and external commutation;
- micro-computer;
- the block of control and signalization.

The essence of this method is following: two signals of unequal and non-industrial frequency are injected into a controlled network relative to ground. The block of current injection into a controlled network may be implemented by means of special transformer included in a network neutral point or via arc suppression reactors with the secondary windings connected to the signal generators.

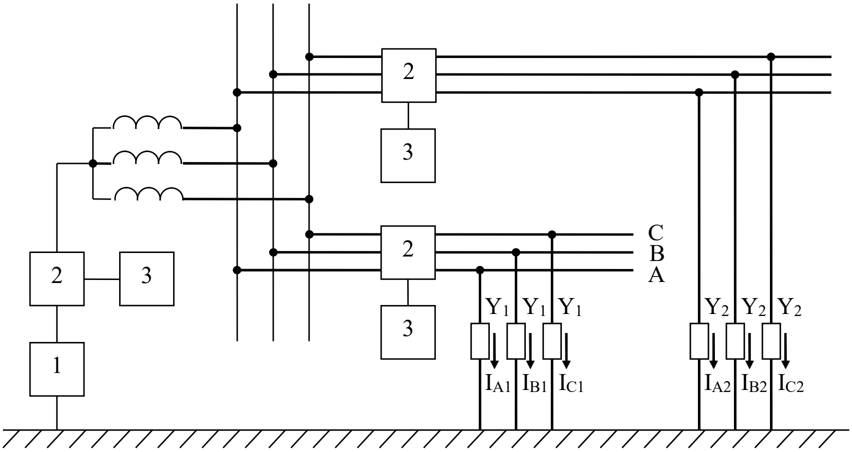

Fig. 4. System of signal injection into the network:
1 – the block of signal injection,
2 – the block of signal extraction and processing, 3 – micro-computer

In controlled sections (connection or line) and at a place of source connection are installed the devices of extraction and processing of appropriate signals, the function of such block could be executed by current and voltage measurement transformers.

For signals injected into a network accepted frequency values are 100 and 200 Hz. This choice is justified by almost complete absence of even harmonics in the network that strongly reduce a measurement error. Depending on the location of measuring current transformer it is possible to measure insulation parameters of particular connection or the whole network.

At the block of signal extraction and processing required frequencies are extracted and converted into digital form then are sent to a calculation unit.

After the simulation calculations in an appropriate computer program, signals are generated, that corresponds to the value of insulation parameters in controlled sections of the power supply system.

Methodology for determination of current parameters is as follows:

complex admittance:

$$\underline{Y} = \frac{1}{R} + j\omega C = \frac{1 + j\omega CR}{R}, \tag{1}$$

and respective impedance:

$$\underline{Z} = \frac{1}{\underline{Y}} = \frac{R}{1 + j\omega CR} = \frac{R(1 - j\omega CR)}{1 + \omega^2 C^2 R^2}. \tag{2}$$

Therefore, the complex current flowing through the resistance:

$$\underline{I} = \frac{U}{R}(1 + j\omega CR) \tag{3}$$

or RMS value:

$$I = \frac{U}{R}\sqrt{1 + \omega^2 C^2 R^2}\ . \tag{4}$$

In case of having two signals, we get the following equation:

$$I_1 = \frac{U_1\sqrt{1 + \omega_1^2 C^2 R^2}}{R}, \tag{5}$$

$$I_2 = \frac{U_2\sqrt{1 + \omega_2^2 C^2 R^2}}{R}, \tag{6}$$

where:

I_1, U_1, ω_1 – current, voltage and frequency of the first signal;
I_2, U_2, ω_2 – current, voltage and frequency for the second signal.

From the formulas (5) and (6) resistance value can be expressed as:

$$R^2 = \frac{U_1^2}{I_1^2 - U_1^2 \omega_1^2 C^2}, \tag{7}$$

$$R^2 = \frac{U_2^2}{I_2^2 - U_2^2 \omega_2^2 C^2}\ . \tag{8}$$

Therefore, for R = const, we can find C:

$$C = \frac{1}{U_1 U_2}\sqrt{\frac{U_2^2 I_1^2 - U_1^2 I_2^2}{\left(\omega_1^2 - \omega_2^2\right)}}\ . \tag{9}$$

Similarly, when C = const we can find R:

$$R = U_1 U_2 \sqrt{\frac{\omega_2^2 - \omega_1^2}{U_2^2 I_1^2 \omega_2^2 - U_1^2 I_2^2 \omega_1^2}}\ . \tag{10}$$

Thus capacitive current can be calculated for the given value of network capacity. An important advantage of the proposed method is versatility for monitoring of fast-changing insulation parameters relative to ground for both the whole network and a given connection [7].

By using the micro-computer this method can be used for:

- operative assessment of insulation resistance and capacitance level for the whole network and each of the connections of distribution or industrial networks;
- measurement of inductance value of an arc-extinguishing coil (compensation device);
- automatic adjustment of compensation device in resonance with the capacity of distribution or industrial network;
- selective signaling of damaged section of the network or protection against ground faults in power supply system regardless of the configuration and neutral point operation mode.

4. CONCLUSIONS

Ground faults, especially under high-resistive condition (e.g. at the simple criteria, based only on the value of ground fault current I_0), cannot be detected in many cases and cleared by power system protection. It is very dangerous for people near the fault location due to possibility of occurrence of full touch and step potentials.

All the time it doing the research of new methods and criteria for the better detection and disconnection of ground faults as well as insulation condition detection. One of these methods is presented in the article, it is based on the simultaneous use of two signals of non-industrial frequency injected into a controlled network. This method allows the selective detection of damaged network section or protection against ground faults in power supply system, regardless of the configuration and neutral point operation mode.

The use of systems that during normal operating conditions of controlled network could detect and localize possible states threatening with a failure allows not only prevention of accidents and people injuries but also avoidance of the costs associated with clearing of the failures.

REFERENCES

[1] HABRYCH M., MIEDZIŃSKI B., WANG XIN, *Applicability of a Hall Sensor in directional ground fault protections of MV cable networks with no-effective earthing*, M. Habrych, B. Miedziński, Xin Wang, Elektronika ir Elektrotechnika, 2016, Vol. 22, No. 5, pp. 26–31.

[2] HÄNNINEN S., *Single phase earth faults in high impedance grounded networks. Characteristics, indication and location*, Technical Research Centre of Finland, Espoo 2001.

[3] ŁUKOWICZ M., *New method of data transmission delay estimation for feeder differential protection*, Present Problems of Power System Control, Vol. 1, 2011, pp. 92–103.

[4] MARCINIAK L., *Wavelet criteria for identification of arc intermittent faults in medium voltage networks*, Proc. of the IS „Modern Electric Power Systems, MEPS '10", paper 09.1, Wrocław, Poland, 2010.

[5] LEI LI, ZHONG Li, *Additional low frequency signal measurement method of insulation resistance about mine cable*, Conference: International Symposium on Computer, Consumer and Control (IS3C), Natl. Chin Yi Univ. Technol, Xian, Peoples Republic of China, Date: Jul. 4–6, 2016, pp. 891–894.
[6] SHKRABETS F., MISYATS Ye., KYRYCHENKO M., *The structure of continuous insulation monitoring system in the 6–10 kV grids in mining enterprises*, The Efficiency and Quality of Industrial Enterprises Power Supply: VI International Scientific and Technical Conference, Publishing Office PSTU, 2008, pp. 401–404 (in Russian).
[7] SHKRABETS F., TSYPLENKOV D., KOVALEV A., KYRYCHENKO M., *Insulation parameters of distribution grids: control and management*, Electrical Engineering and Electromechanics, Issue 1, 2010, pp. 49–51 (in Russian).

switching arc DC,
low voltage and low power installation,
arc-to-glow transition

Grzegorz WIŚNIEWSKI*

ARC TO GLOW TRANSITION FOR USING DC LOW POWER SWITCHES IN LOW VOLTAGE ELECTRIC GRIDS

This paper presents and discusses results of analysis and investigations of arc to glow transformation phenomenon at contact opening, under DC inductive loads of low power (≤10 J) and low voltage (≤250 V). The proportion in duration of arcing and glowing is investigated in dependence on current and voltage value, contact material properties. The transition phenomenon is analyzed by means of fast photography and emission spectroscopy to complete the study. On the basis of investigated results the conclusions about the possibility of control of the arc to glow transformation for practical use in DC low voltage and low power electrical grids are formulated.

1. INTRODUCTION

Recently can be seen a rising interest in using the DC grids in residential houses. This is due to increasing application of renewable DC energy sources (mainly photovoltaic cells) and the tendency to reduce both wiring and utility costs by elimination a lot of DC/AC power supplies and electronic power converters to one central power supply. Moreover, the market offers full gamma of various kinds of electrical devices powered DC, mainly various types of LED light sources. It is therefore recommended (especially in residential buildings) an implementation of additional, separate DC installation (Fig. 1) however, adapted in a case, for connection to an AC primary site as proposed, for example in [1]. However, the use of the DC power source is related to serious disadvantage resulted primarily with the inability of its transformation into different voltage levels, although dominated by standardizing 5 V for USB power supply. Hence, there is a need for transferring and switching currents of relatively

* Wrocław University of Science and Technology, Department of Electrical Power Engineering, Wybrzeże Wyspiańskiego, 27, 50-370 Wrocław, Poland, e-mail: grzegorz.wisniewski@pwr.edu.pl

higher values and energy. Effective switching of DC loads needs the use of both special semiconductor and/or hybrid devices with the overvoltage protection.

Fig. 1. Wall socket with dual USB interface and electrical outlet

In certain applications, however, particularly under small values of currents and where the breaking speed is not important the contact switches are equipped with damping resistors [2]. However, during breaking inductive loads the switching arc duration can be prolonged significantly and can lead, as result, to rapid damage of the switch and contacts. Studies of the arcing under low voltage DC showed that in a number of cases it can be found advantageous effect of spontaneous transition of the arc into glow discharge. This reduces the erosion of contacts surface and increases considerably, as a result, the electrical life of the switch at a very effective limitation (often to zero) the switching overvoltage values [3,4]. The duration of the glow discharge is of course dependent on the energy of the inductive circuit therefore in some cases, it is necessary to use its forced limitation. However, in most applications there is no such necessity. The problem, however, remains the practical implementation of the switch structure so that you could predictable control the transition of DC switching arc in glow discharge as fast as possible after the opening of the contacts. The question is tough because of the complexity of mutually interacting phenomena within the contact gap associated with the electrical discharge. It is thus found either a fast transformation of initial unstable electrical pre-arc in the glow discharge, or his initiation after a while of burning arc duration or at all lack of glow discharge. Thus the efficiency of the transformation process changes during switching, but fortunately there is a statistically predictable. This is primarily due to the difficulty in maintaining the same reproducible physical-chemical conditions as on the contact surfaces as well as within a relatively small gap area between the contacts. Some explanations of the conditions of instability provide a mathematical description of this effect based on the experimental results obtained [4]. The article presents and discusses the results of experimental studies of transition effect of switching DC arc in a glow discharge when interrupting a DC inductive current of low power (≤10 J) and low voltage (≤250 V). The study concerned the impact of such factors like, current and voltage value, inductive energy of switching circuit and selected parameters of the switch. Particular emphasis is placed on the selection of contact material. Based on the results of experimental study using, among other things, fast photography and spectroscopy for the implementation of the arc to glow transition effect in selected contact switches of a low power and low voltage DC.

2. THEORETICAL EVALUATION OF THE ARC TO GLOW TRANSITION

The study showed that a glow discharge appears under unstable burning of the arc and can be initiated or almost immediately after the start of the opening the contact and/or after some time of the arc existence. Approximate theoretical analysis of the arc transition in a glow discharge (for the electric circuit as shown in Fig. 2) is given in detail in [6].

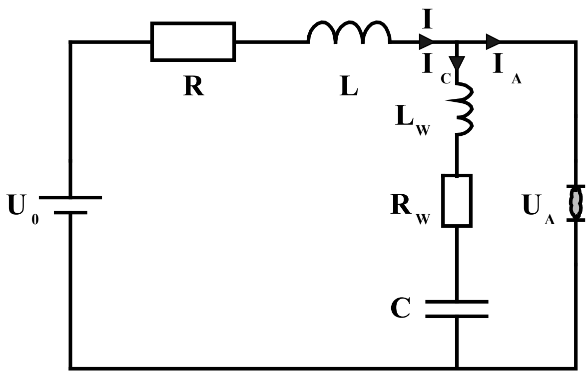

Fig. 2. Electrical circuit diagram of the test rig: U_0, I – supplied voltage and load current; U_A – arc voltage; R, L, C – load resistance, inductance and circuit capacity; L_W, R_W – wires inductance and resistance respectively

On the basis of the investigated results [3, 4, 6] the process of contact opening, associated with arc to glow discharge, can be presented in four stages representing different phenomena [4] as illustrated in Fig. 3. The stage I (pre-arcing) is related to the initial conditions for arc ignition in particular the values of current, voltage, density of evaporated metallic particles from contacts, length of contact gap, as well as electric field intensity that are important for further arc evaluation. According to different temperature value in the contact spot, one can distinguish here, three intervals as follows: first-from initial to softening temperature (elastic restitution); second-from softening to melting (plastic deformation) and third-from melting to boiling temperature (bridging) respectively. Since the first two parts are of a very short duration in our case (under consideration) thus, a liquid contact bridge is the most important factor for the further arc development. There are two existing mechanisms of the bridge formation and its dynamics strongly related to physical properties of contact material. The first one corresponds to a bridge formation due to melting of a micro-asperity on the contact surface, whereas the second is due to the extension of a liquid drop from the melted area in the constriction zone [4].

This drop extension mechanism of the bridge formation is typical for low-melting point metals with high thermal conductivity like silver and its compositions. Therefore, for such contact materials the length and duration of the ruptured bridge (t_b in Fig. 3) is large enough to provide thermal ionization of metal vapours needed for the arc ignition [5].

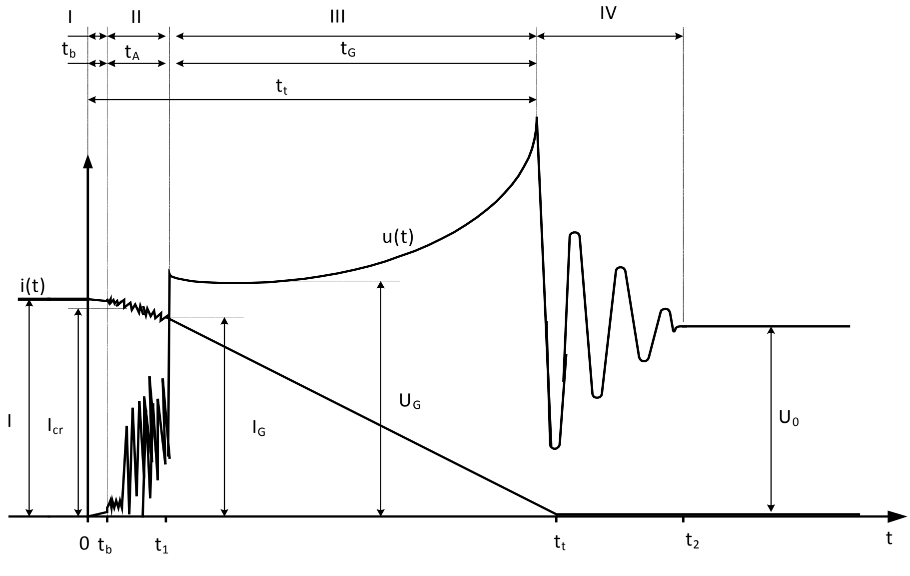

Fig. 3. Illustration of voltage current characteristics at contact opening:
t_t, t_G, t_A, t_b, t_{cr} – total, glowing, arc discharge, bridge and critical arc time, respectively;
U_0, U_g – supply and glow voltage; I_{cr}, I_G – critical arc and glow transition current, respectively

The further evaporation is also enough sufficient to maintain stable arc of a relatively long duration (extended stage II – Fig. 3). Therefore, silver and its compositions are not suitable for the arc to glow applications what was confirmed by experiment. On the contrary the micro-asperity genesis seems to be peculiar for more refractory metals such as nickel. The quantity of vapours of micro-asperity is not sufficient for stable arc ignition and its occurs because of field emission breakdown and/or air avalanches breakdown. The bridge is in such case significantly reduced or even invisible.

Sometimes it may be accompanied by showering phenomena and/or explosive electron emission (ecton process). As a result the arc duration at this mechanism of bridge formation is small and depends on the pressure according to Pashen's law [2]. When the decreasing current reaches the certain critical value I_{cr} at the critical time t_{cr} the arc becomes unstable therefore, even a very small perturbation of current or voltage may cause the arc collapse (see Fig. 3.).

3. EXPERYMENTAL INVESTIGATIONS

3.1. TESTING PROCEDURE

In order to conduct research a special testing system equipped with a dismountable hermetic chamber with the contact system inside, controlled by a PC was designed and assembled as in Fig.4.

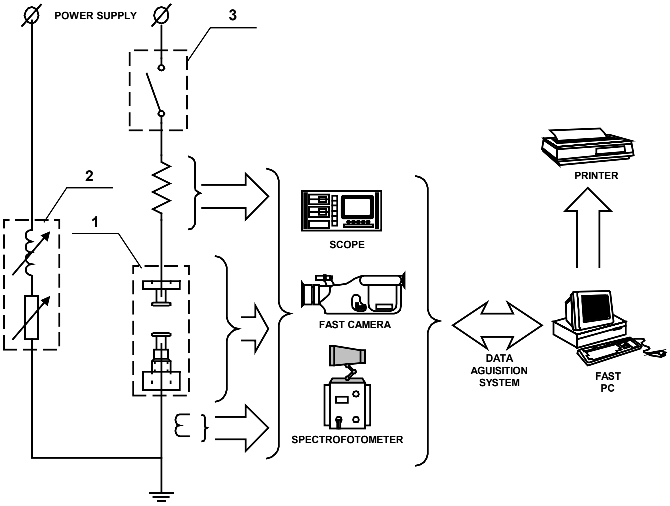

Fig. 4. Schematic set-up of the test apparatus: 1 – dismountable chamber stand, 2 – load to be adjusted, 3 – auxiliary protection switch

Plain, round contacts (5 mm in diameter and 1 mm of thickness) operated in gaseous medium under normal pressure. As a contact material were used different both refractory and non-refractory fine metals (like W, Mo, Ni, Ti, and Ta), selected fine powder tungsten-copper sinters (with some additives like Co 2%) and vapour deposited copper molybdenum and copper chromium compositions. Contacts opening velocity was ranged from 0.04 m/s up to about 0.4 m/s at contact force from 0.6 N up to around 40 N. During the study with the use of fast photography (2200 frames per second) and radiation spectra measurements the length of contact gap was enlarged up to about 7 mm (from 2.5 mm). Due to the limitation of performance in transient of the selected fiber-optics spectrometer (time spectrum analysis about 200 ms) the research of emission spectrum (in visible light range from 300 nm to 750 nm) was carried out for separately generated arc and glow discharges produced under the DC inductive load breaking. The investigations were performed for currents in the range of 0.5–3.0 A at voltage from 48 V to 250 V and at a circuit time constant varied from 10 ms up to 40 ms (discharge energy less than 10 J). The voltage, current, discharge power and the contact gap length variation were respectively recorded. To reduce the influence of surface contaminations, the contacts were preliminary mechanically and chemically cleaned and subjected to preliminary operation before testing. Ten samples for each contact material were selected and mean values and predicted ranges with 95% level of confidence were calculated after completed testing.

3.2. CONTACT MATERIAL EFFECT

The study showed that effect of transition of the arc discharge in a glowing is primarily dependent on contact material applied. However, it is noticeable for both refractory as well as non-refractory different materials under specified conditions of operation no less for materials such as silver and its alloys it is unattainable. It has been also found, that for consecutive switching under identical conditions, the transition is not identical but similar. It reveals that, some of the mechanisms depend on the probability of various events and therefore, the arc to glow transformation is not completely determined, but is subject to the lows of probability. The glow discharge at contact opening is found to arise most easily when fine nickel is applied. It can be attainable

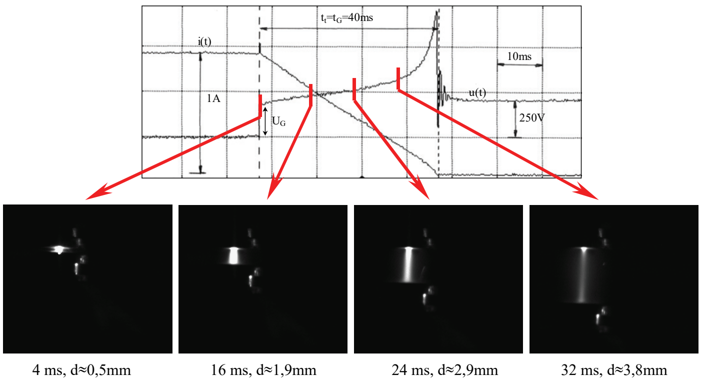

Fig. 5. Glow discharge triggered at the beginning of the contact separation
when breake inductive load DC (250 V, 1 A, 40 ms) in air (~100 kPa) with contacts made of fine nickel:
t_t, t_G – total and glowing time respectively, U_G – glow voltage

even at the beginning of contact displacement (at the moment of bridge evaporation or protrusions explosion) as illustrated in Fig. 5. As a result, the discharge energy within the contact area is dissipated at a much higher voltage level (U_G about 300 V) and for current decreasing almost linearly with time.

Therefore, both contact erosion and switching over-voltage values are reduced significantly. However, the glowing is usually generated due to transition from very unstable arc discharge (short arc, showering arc) which can be compared from Figs. 6 and 7.

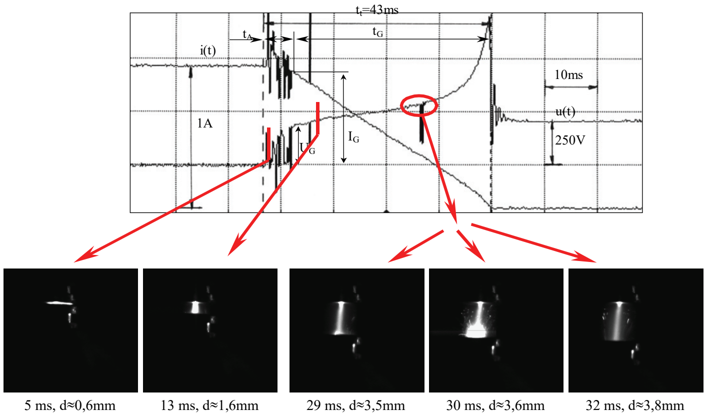

Fig. 6. The unstable arc to glow transition when use the nickel contacts (250 V, 1 A, 40 ms, air ~100 kPa): t_t, t_A, t_G – total, arcing and glow discharge time, respectively; U_G – glow voltage, I_G – arc to glow transformation current value

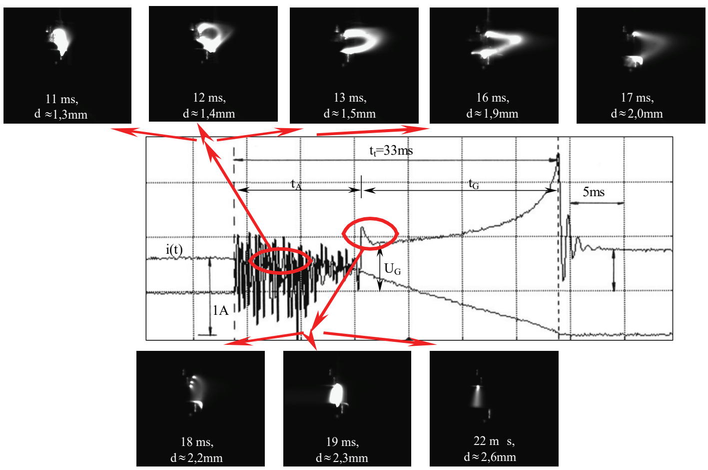

Fig. 7. Development of the electrical discharge when use contacts made of fine molybdenum (250, 0.5 A, 40 ms, in air under 100 kPa)

In these cases the discharge tends to lead to occasional arcing due to explosive erosion from the cathode (see 30 ms for gap ≈3.6 mm in Fig. 6). This is related to a sudden change of the cathode surface conditions and associated reinforced emission, which confirms the major role of this electrode. For the contacts made of refractory materials like tungsten or molybdenum the arc to glow transformation can also be obtained. However, the extensive unstable arcing can be seen even for relatively low current values being broken as demonstrated in Fig. 7. Oxidation of the contact surface in air at an elevated temperature does not seem to be a major stimulating factor. Besides, it is worth noting that just at the transition moment, the anodic spot may be split into a few separate parts (see three spots at 18 ms in Fig. 7). It appears that the diffused anodic arc or multi-spot glowing confirms the importance of the anode as well and complexity of the problem. It should also be noted that the arc to glow transition can be initiated at a current (I_G) higher than so called "minimum arcing" current values (I_{cr}) for the applied contact materials [2]. This is particularly visible for fine nickel where ratio I_G/I_{cr} value can reach up to about 2.5. For example, the materials commonly used like fine copper and derivatives (brass), likewise silver and its compositions are found useless as a contact material to make USB connectors, since the electric discharge within the contact gap area is usually dominated by a stable electric arc [7, 8]. However, for copper-molybdenum condensed materials, with the increase of the molybdenum content (under the test up to about 14%) the arc to glow transition is visible, but with a small portion of glow duration. The contribution of gaseous elements (when operated in air) in arc radiation intensity is about 60% which indicates the existence of both metallic and gaseous arc phases (see Fig. 8).

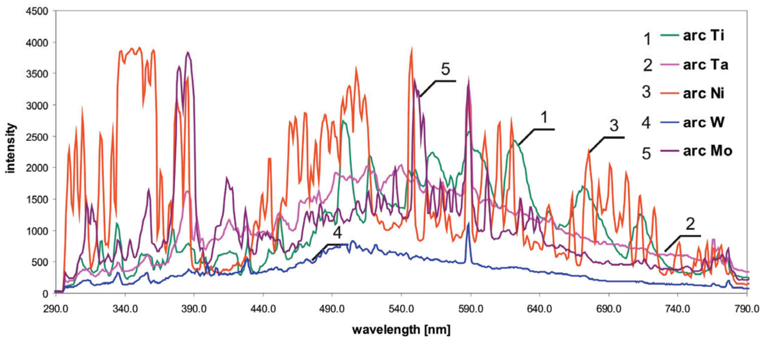

Fig. 8. Radiation spectrum of breaking arc in air under normal pressure for contacts made of different fine materials (Ti, Ta, Ni, W, Mo)

Intensity of the glowing radiation is about 10-times lower and exhibits an identical picture, independently of the contact material what can be compared from Fig. 9. The contribution of the electrodes elements under glowing, which is about 14%, results most probably from the fact that the metallic vapours inject into the gap area at the moment of bridge or protrusion explosion. For the given stored circuit inductive energy (circuit time constant) the total discharge time (t_t) was found to be almost independent on the quenching medium pressure.

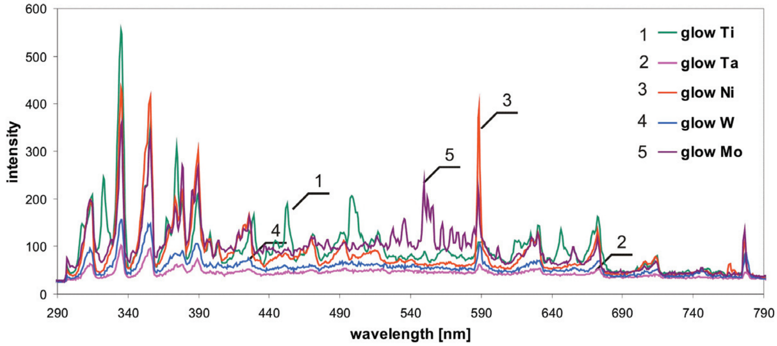

Fig. 9. Radiation spectrum for glowing discharge at contact opening in air for different fine contact materials (Ti, Ta, Ni, W, Mo)

The total discharge time t_t as well as the portion of the glow duration is also enhanced by the increased supply voltage what for different contact material is illustrated in Fig 10.

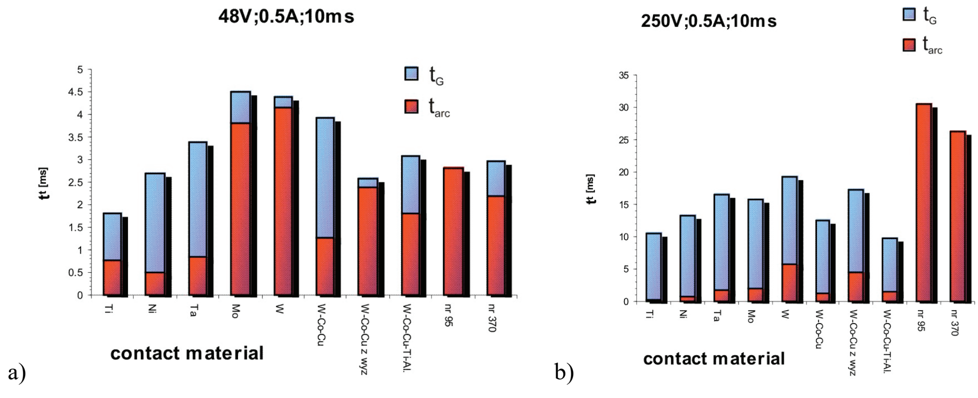

Fig. 10. Comparison of total discharge time (t_t) and portion of the glow duration (t_G) for tested contact materials when interrupt inductive load DC (0.5 A, 10 ms) at different voltage value (48 V and 250 V) in air under normal pressure (~100 kPa)

The best results are obtained for the fine nickel contacts. However, titanium seems to be promising as well particularly as dopant for fine powder sinters [6]. The portion of the glow duration here, is the highest under the same conditions of operation which reduces surface erosion significantly. The surface topography inspection, as well as a microstructure analysis, indicate that in a case when the arc-glow transition occurs easily the erosion is less extensive. For example, for pure nickel the eroded area of the contact surface (particularly the anode) after about 300 switching was found to be significantly smaller than after 40 switches with predominant arcing [3, 6]. This is equivalent to an increase in electrical life of the switch.

4. CONCLUSION

The occurrence of glow discharge and/or transition of the switching arc in a glowing observed in inductive circuits of low voltage and low power is an advantages because it decreases significantly erosion of the contact surfaces, thus extending the switch life, reducing simultaneously the voltage surge values.

Thus, although repeatability of as current as well as switching voltage waveforms at each successive cycle is not satisfied but, statistically the transition of arc in a glow discharge will be achieved. However, the transition can be obtained for any low voltage and low power contact switch, operating even in open air, but it is particularly recommended for auxiliary encapsulated (hermetic) switches of a compact structure, in which many interfering effects such as oxidation, contamination etc. can be reduced or even eliminated.

REFERENCES

[1] MECKLER J.P., GERDINAND F., WEISS R., BOEKE U., MAUER A., *Hybrid switches in protective devices for low-voltage DC grids at commercial used buildings*, Proc. of 27th Int. Conf. on Electric Contacts, June 22–26, 2014, Dresden, Germany, 2014, pp. 120–125.

[2] HOLM R., *Electric contacts. Theory and applications*, M. Dekker (Ed.), Basel, Switzerland, 1999.

[3] MIEDZINSKI B., SZYMANSKI A., WISNIEWSKI G., GRODZINSKI A., *Transformation of low power arc to glowing under inductive load DC*, Proc. Int. Conf. SAP 2001, Łódź, Poland, 17–20.09.2001, pp. 117–120.

[4] KHARIN S.N., NOURI H., MIEDZINSKI B., WISNIEWSKI G., *Transient phenomena of arc to glow discharge transformation at contact opening*, Proc. of 21st Int. Conf. on Electric Contacts, Zurich, Switzerland, 9–12.09.2002, pp. 425–431.

[5] KHARIN S.N., *Mathematical model of the arc evaluation from metallic phase to gaseous phase*, Proc. 20th Int. Conf. on Electric Contacts, Stockholm, Sweden, 2000, pp. 155–160.

[6] NOURI H., MIEDZINSKI B., KHARIN S.N., WISNIEWSKI G., *Analysis and investigations of arc to glow discharge transformation under DC inductive load*, Mechanizacja i Automatyzacja Górnictwa MIAG, No. 8/439, 2007, pp. 7–22.

[7] MIEDZINSKI B., WISNIEWSKI G., SHOFFA V.N., GRECHANYUK N.I., *Performance of copper-molybdenum contacts when used for inductive DC load*, Electrical Contacts and Electrodes, Institute of Material Science, 2004, pp. 19–23.

[8] KHARIN S.N., NOURI H., DAVIES T., *Influence of Inductance on the Arc Evolution in AgMeO Electrical Contacts*, Proc. 48th IEEE Holm Conf. on Electrical Contacts, Orlando, USA, 2002, pp. 108–119.

Proton Exchange Membrane (PEM) Fuel Cell,
DC/DC boost converter, Distributed Generation (DG),
polarization curve, efficiency

Sunny KATYARA*, Jan IŻYKOWSKI**,
Łukasz STASZEWSKI**, Fawad SHAIKH*

TECHNICAL AND ECONOMICAL EVALUATION OF PROTON EXCHANGE MEMBRANE (PEM) FUEL CELL FOR COMMERCIAL APPLICATIONS

The green energy sources are the utmost needs of today's world where the reserves of fossil fuel are depleting day by day. The Distributed Generation (DG) has become integral part of power system at commercial level. The most efficient among all DGs and Renewable Energy Sources (RES) is the Fuel Cell (FC) power generation. The fuel cell invariably converts chemical energy directly into electricity. The Fuel cells have normally 60 to 70% efficiency at working conditions. The polarization curve of fuel cell plays important role in improving its efficiency.

This research presents the mathematical and Simulink modeling 6 kW, 45 V_{dc} of Proton Exchange Membrane (PEM) fuel cell. The input thermodynamic parameters of fuel cell are varied and their effects on the output electrical variable are observed. The DC/DC boost converter is used to step up the voltage of fuel cell to 100 V_{dc} at commercial usable level. A new mathematical equation is presented to improve the efficiency of fuel. The mathematical results are then varied through Simulink results.

1. INTRODUCTION

The fuel cell is an electromechanical device which transforms the chemical energy into electricity. Due to its higher efficiency, fuel cell is widely being accepted for power generation as compared to electromechanical devices. The fuel cell does not involve any intermediate link between the conversion processes [1]. However the growing issues of global warming has resulted in the alarming situation for the world

* Electrical Engineering, Sukkur IBA University, Pakistan, e-mail: sunny.katyara@iba-suk.edu.pk, mfawad.be14@iba-suk.edu.pk

** Department of Electrical Power Engineering, Wrocław University of Science and Technology, Poland, e-mail: jan.izykowski@pwr.edu.pl, lukasz.staszewski@pwr.edu.pl

to use clean energy sources for power generation [2]. The fuel cell generation is free from CO_2 emissions.

Figure 1 shows the basic construction and working of fuel cell. Basically a fuel has three adjacent segments:

a. Anode;
b. Cathode;
c. Electrolyte.

The fuel used in cell is the hydrogen gas, which is being supplied to the anode. At anode the catalyst oxidizes the hydrogen into positive ion (H^+) with release of electron. The electrolyte is the substance especially designed so that ions can pass through it but electrons cannot. The free electrons then pass through load thus creating electricity. The positively charged hydrogen ion (H^+)

The Proton Exchange Membrane (PEM) fuel cell is the most commonly used fuel cell for commercial applications due to its best voltage and current characteristics. It is small in size, weighs low and has least corrosion. The PEM fuel cell operates at temperature range between 35 °C to 100 °C. Its transient response is quick as compared to Solid Oxide fuel cell which works at temperature above 700 °C.

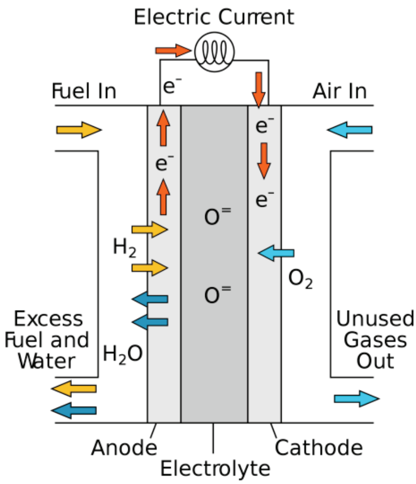

Fig. 1. Proton Exchange Membrane (PEM) Fuel Cell

In this area, the work has been done to certain extent. Aziz et. al (2011) analyzed the working performance of 3.757 kW PEM fuel cell at load current of 261.4 A. The cell was investigated under the transient as well as under steady states. Outeiro et. al (2011) developed the Simulink model of PEM fuel cell and evaluated the optimization of cell using Simulated Annealing (SA) algorithm. The design specifications of DC/DC converter were also considered for boost up process at commercial level. Ibrahim et. al (2015) deduced the new mathematical model for investigating the characteristics of PEM fuel cell. The input parameters to the model were thermodynamic and outputs were electrical. Wee et al (2006) applied PEM fuel cell in the real time applications such as automotive vehicles. He also enumerated the working merits of fuel cell technology for energy production.

This research work develops an electrochemical model of PEM fuel cell based on ballard group to simulate and analyze the transient response of cell voltage, flow rates of hydrogen and oxygen, temperature of fuel cell and pressure at anode and cathode under sudden changes in the load current of PEM fuel cell. The MATLAB model of PEM fuel cell helps to estimate the maximum power produced by the cell and to prevent cell from excessive heat, thereby notifying the temperature limits.

2. RESEARCH METHODOLOGY

A. Mathematical Model

The mathematical model for PEM fuel cell is shown in Fig. 1. The model is used to analyze the static and dynamic characteristics of PEM fuel cell.

According to Kirchhoff's voltage law, the output voltage of single PEM fuel cell can be found by Eq. (1)

$$V_F = E_{NL} - V_{RA} - V_{RC} - V_{RO} \tag{1}$$

where:

V_F – output fuel cell voltage,

E_{NL} – no load voltage of fuel cell,

V_{RA} – voltage drop due to activation loss,

V_{RC} – voltage drop due to concentration loss,

V_{R0} – voltage drop due to ohmic loss.

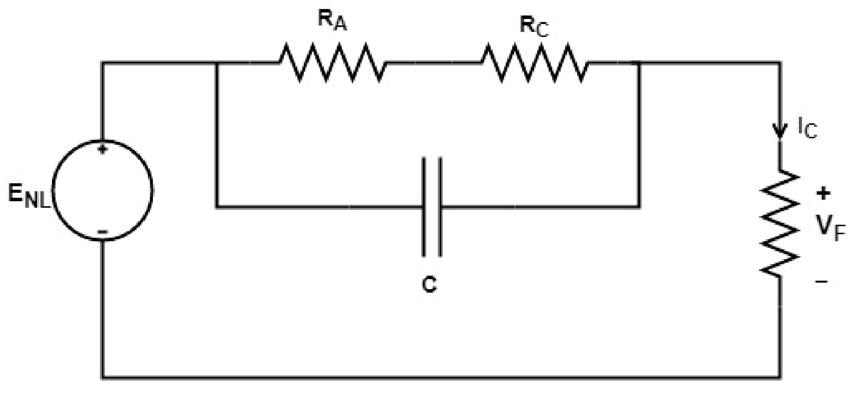

Fig. 1. Simplified electrochemical model of PEM fuel cell

The no load voltage of fuel cell defines its reversible voltage and is given by Eq. (2)

$$E_{NL} = 1.23 - 8.5 \times 10^{-3} \times (T - 298) + 4.31 \times 10^{-5} \times \left[\ln(P_1) + \frac{1}{2}(P_2) \right] \tag{2}$$

where:

P_1 – partial pressure of hydrogen,
P_2 – partial pressure of oxygen,
T – temperature of cell.

The voltage drop due to activation loss is given by the Eq. (3)

$$V_{RA} = -[\ell_1 + \ell_2 \times T + \ell 3 \times T \times \ln(CO_2)] \tag{3}$$

2. RESULTS AND DISCUSSION

Figure 1 shows the complete model of fuel cell stack that produce 6 kW and 45 V DC. The DC to DC Boost converter regulates the voltage up to 100 V and it is loaded with RL load to visualize the real time scenario. The simulation was performed to obtain the results of variations in the efficiency of fuel cell when input parameters to fuel cell get changed. Initially for 10 sec, the input to fuel cell was constant but after 10 sec switch changes the position and input parameters started changing such as fuel flow rate changes from 50 lpm (liter per minute) to 85 lpm.

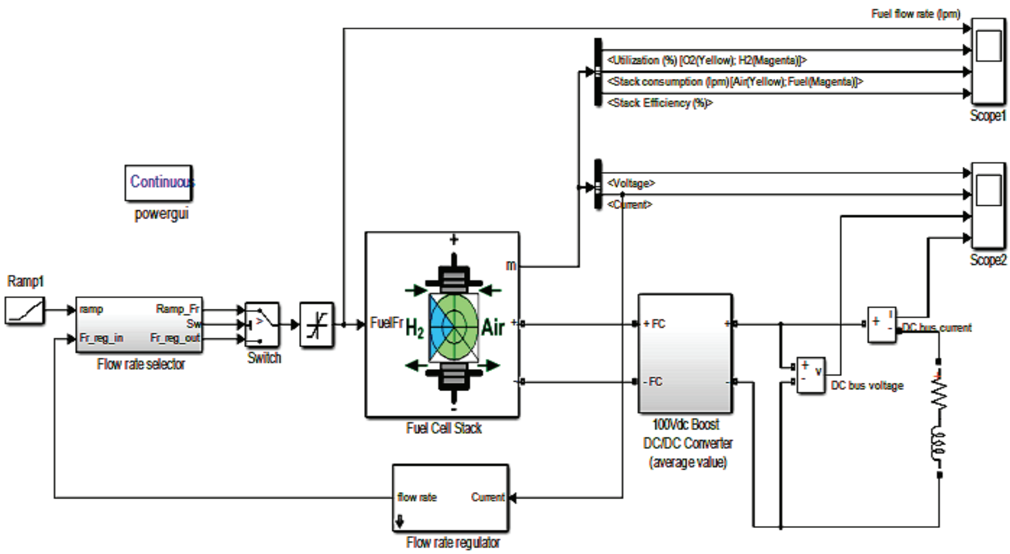

Fig. 2. Simulink model of PEM fuel cell stack

an

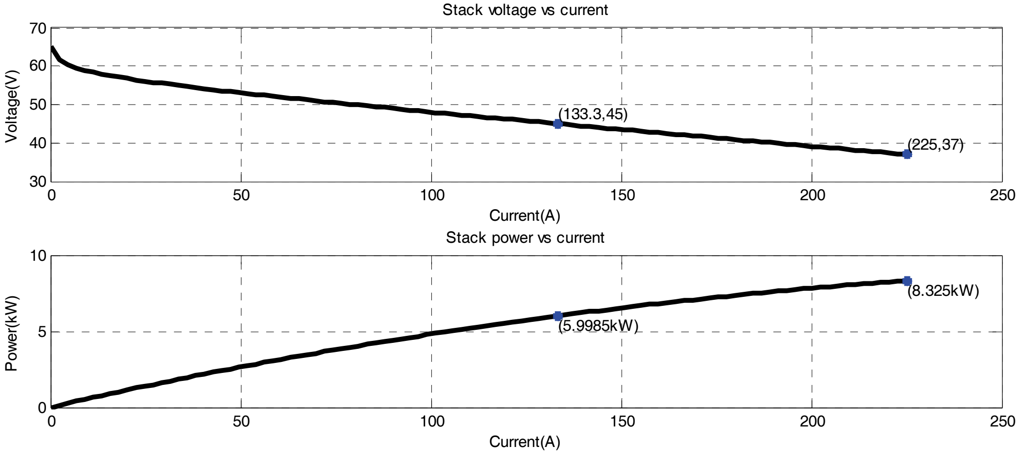

Fig. 2. Polarization curve of fuel cell

Figure 2 shows the polarization curve of fuel cell which indicates variation of its resistance with its charge flows. Due to inverse characteristics of fuel cell, causes increased voltage drop due to increased internal chemical losses. In the first region, which is called activation region, the drop of voltage is due to slowness of chemical reaction at the surface of electrodes. The width of activation region depends upon the temperature and operating pressure in the system and so as the electrode types and catalyst are selected. The second region, which is called ohmic region indicates the resistive losses due to internal resistance materials used in fuel cell stack like; anode,

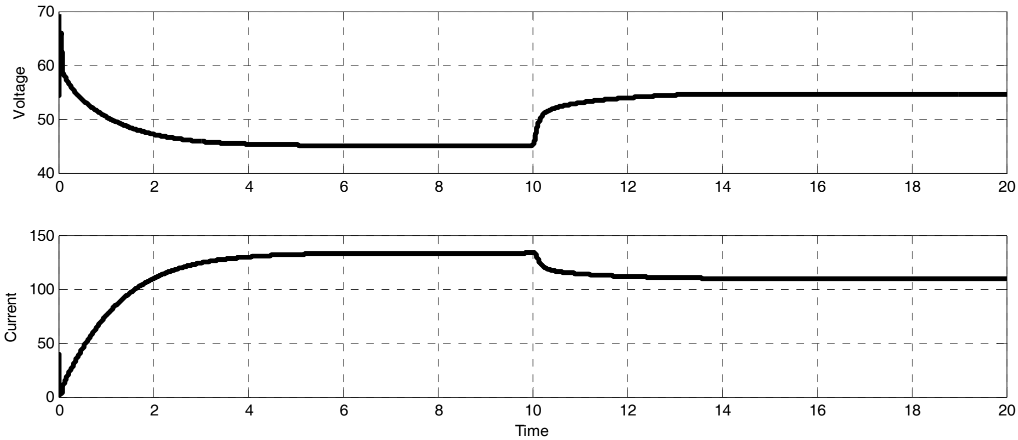

Fig. 3. Fuel cell stack voltage and current

cathode and electrolyte. Finally, the third region is called concentration region, which indicates mass transport losses due to change in concentration of reactants, as the fuel get used up in the stack. Figure 3 shows the output voltage and current of fuel cell.

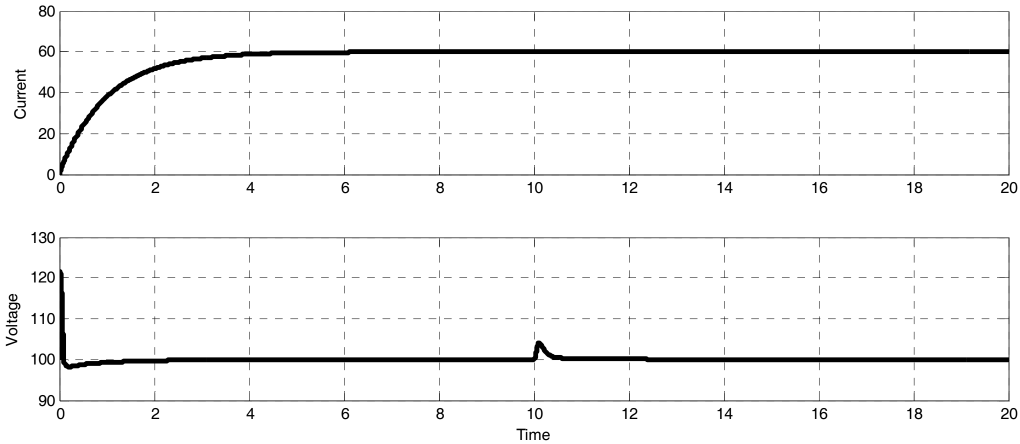

Fig. 4. Voltage and current for DC/DC boost converter

The output voltage of fuel cell is low therefore boost converter is used to step up the DC voltage and also to regulate its output as shown in Fig. 4. Initially at the of start of simulation there is a peak up to 122 volts due to least drop but as inductor opposes change in current and also transfer function interfaced with the pulses of IGBT, makes it stable and voltage remain constant. After 10 sec, the fuel supply is being

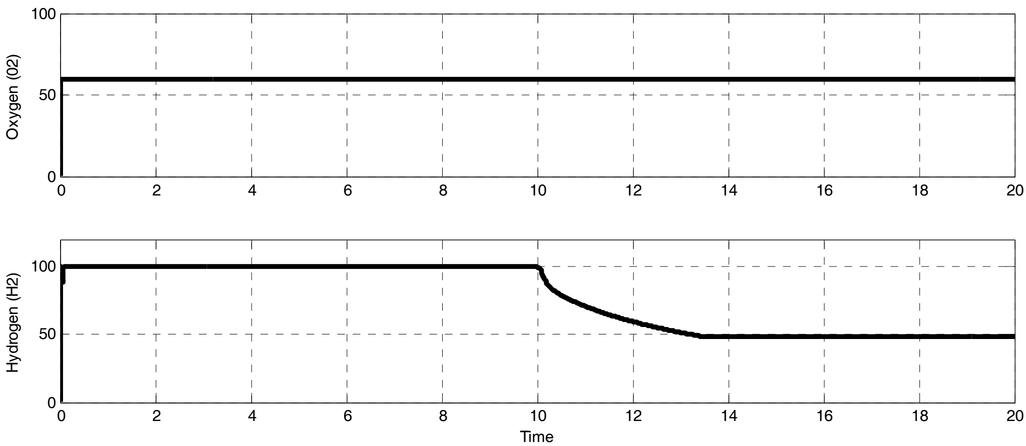

Fig. 5. Utilization of hydrogen and oxygen

increased resulting increase in voltage but regulator makes it stable within 10th sec and voltage at the load.

Figure 5 shows that how much oxygen and hydrogen is being supplied to the stack. Since 99.56% of hydrogen from tank is being supplied to the fuel cell with a constant use of 60% oxygen as shown in Fig. 6. It shows that how much H_2 and O_2 are consumed to give output. As flow rate varies then there should be variations.

The slow reaction in fuel cell gave more voltage so its flow rate increases and its stability reaction decreases. Therefore, due to this consumption of hydrogen, the efficiency of fuel reduces as shown in Fig. 7.

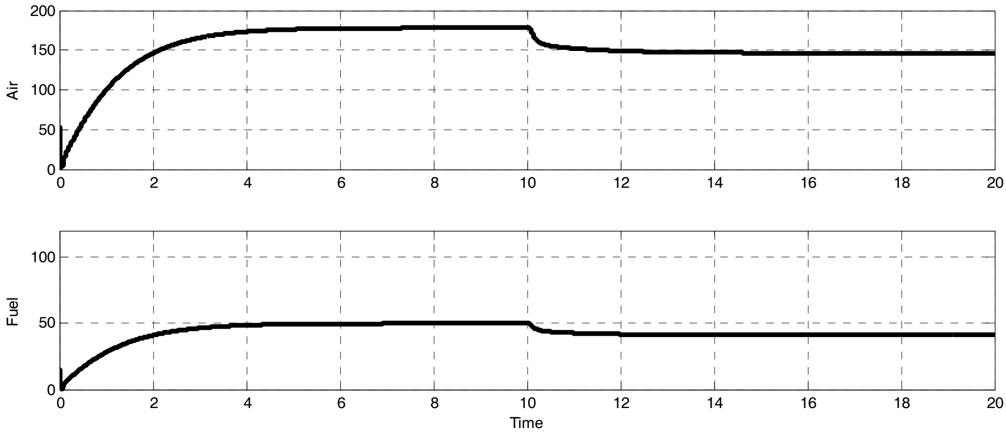

Fig. 6. Fuel stack consumption for air and fuel

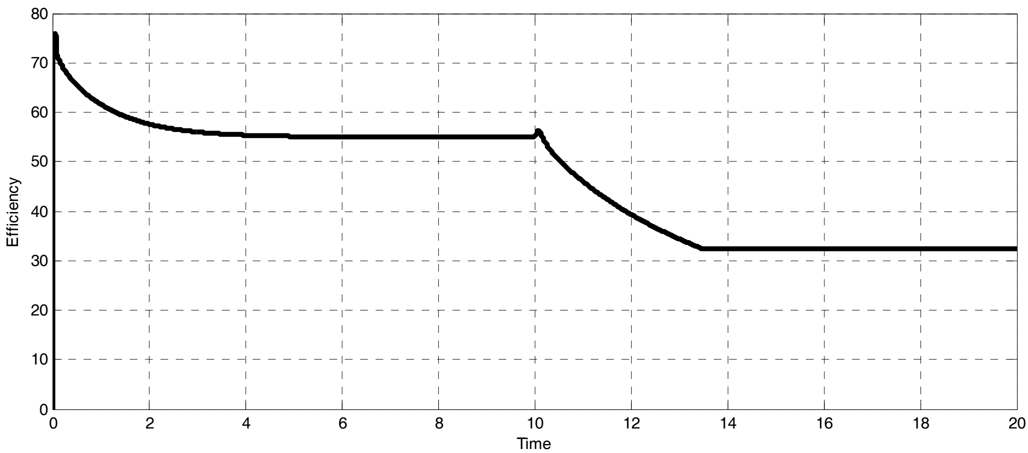

Fig. 7. Fuel cell efficiency

The efficiency of tested PEM cell is 55% but when fuel flow rate is slow, its efficiency reduces up to 32%. When fuel flow rate is slow, the rate of reaction is low and the stack does not get fully activated as shown in Fig, 7. Also, if the rate of fuel is increased, the fuel cell is not capable of utilizing the entire fuel simultaneously resulting input fuel is high and output is low, so overall efficiency is reduced. Therefore, the fuel cell should be operated within the saturation dome of its characteristics, in order to get the maximum efficiency,

3. CONCLUSION

The fossil fuel reserves are depleting day by day and they also badly effect the environment because they are the major cause of CO_2 emission. Renewable source is the best way to overcome from these problems. The renewable resource with the highest efficiency is fuel cell we can get up to 60% to 70% efficiency from the fuel cell. In this paper mathematical model is observed to improve the efficiency of fuel cell and equations are defined to analyze the fuel cell from different aspect this model is capable to analyze the dynamic and static characteristics of PEM Fuel cell. We use MATLAB Simulink to model the PEM fuel cell and vary the different parameter like increase the amount of fuel and then different output parameter are observed such as fuel consumption and utilization, voltage, current and efficiency. We observed that increase the amount of fuel cause the efficiency negatively because fuel cells are defined for particular fuel flow rate, to overcome from this problem fuel flow rate should me with in permissible limits to get the highest efficiency

FUTURE RECOMMENDATIONS

The fuel cell with its portable nature can be used for Army purposes to power the auxiliaries of jets and tanks during the war when national grids are inaccessible. Also, fuel cell with its high efficiency can be used in small scale automobiles to beat the increasing process of fossil fuels. In future, the fuel cell technology will play an important in energy harvesting. It will recycle its own exhaust with pyrolyses, to generate additional energy.

ACKNOWLEDGEMENT

Authors are very much thankful to Sukkur IBA University for providing peaceful environment for conducting this research work.

REFRENCES

[1] CORRÊA J.M., FARRET F.A., POPOV V.A., SIMÕES M.G., *Sensitivity analysis of the modeling parameters used in simulation of proton exchange membrane fuel cells*, IEEE Transactions on Energy Conversion, 2005, 1(20), 211–218.

[2] OUTEIRO M.T., CHIBANTE R., CARVALHO A.S., DE ALMEIDA A.T., *A new parameter extraction method for accurate modeling of PEM fuel cells*, International Journal of Energy Research, 2008, 33(11), pp. 978–988.
[3] CHANGCHIEN S.K., LIANG T.J., CHEN J.F., YANG L.S., *Novel high step-up DC–DC converter for fuel cell energy conversion system*, IEE Trans. Ind. Electron., June 2010, Vol. 57, No. 6, pp. 2007–2017.
[4] HUANG X., ZHANG Z., JIANG J., *Fuel cell technology for distributed generation: an overview*, IEEE Symposium on Industrial Electron, 2006, pp. 1613–1618.
[5] CHOI T., LEE K.Y., *Interface of a fuel cell distributed generator with distribution system network*, [in:] Proc. of the IEEE Power Energy Society General Meeting, Calgary, Canada, July 26–30, 2009.
[6] WANG C., NEHRIR M., *Dynamic models and model validation for PEM fuel cells using electrical circuits*, IEEE Transactions on Energy Conversion, 2005, 2(20), p. 442–451.
[7] ZEHRA URAL, MUHSIN TUNAY GENCOGLU, BILAL GUMUS, *Dynamic Simulation of a PEM Fuel Cell System*, Proceedings 2nd International Hydrogen Energy Congress and Exhibition, IHEC 2007.
[8] SEYEZHAI R., MATHUR B.L., *Mathematical Modeling of Proton Exchange Membrane Fuel Cell*, International Journal of Computer Applications (0975–8887), April 2011, Vol. 20, No. 5.
[9] IBRAHIM M.M. SALEH R. ALI, ZHANG H., *Simplified mathematical model of proton exchange membrane fuel cell based on horizon fuel cell stack*, J. Mod. Power Syst. Clean Energy, 2016, 4(4), 668–679.
[10] QIU J., DONG Z.Y., ZHAO J.H. et al., *A low-carbon oriented probabilistic approach for transmission expansion planning*, Power Syst. Clean Energ., 2015, 3(1), 14–23, DOI: 10.1007/s40565-015-0105-3.
[11] CORRÊA J.M., FARRET F.A., CANHA L.N., *An analysis of the dynamic performance of proton exchange membrane fuel cells using an electrochemical model*, 27th Annual Conference on the IEEE Industrial Electronics Society, 2001.
[12] FORRAI H.F., YANAGITA Y., KATO Y., *Fuel-cell parameter estimation and diagnostics*, IEEE Transactions on Energy Conversion, 2005, 3(20), 668–675.
[13] CHOI W., ENJETI P.N., HOWZE J.W., *Development of an equivalent circuit model of a fuel cell to evaluate the effects of inverter ripple current*, IEEE Transactions on Energy Conversion, 2004, Vol. 45, pp. 456–465.
[14] MANISH KHEMARIYA, ARVIND MITTAL, *Modeling and Simulation of different components of a standalone Photovoltaic and PEM Fuel Cell Hybrid System*, International Journal on Emerging Technologies, 2010.
[15] EL-SHARKH M.Y., RAHMAN A., ALAM M.S., *A dynamic model for a stand-alone PEM fuel cell power plant for residential applications*, J. Power Sources, 2004, 138(1/2), 199–204.
[16] YUAN W., TANG Y., PAN M.Q., *Model prediction of effects of operating parameters on proton exchange membrane fuel cell performance*, Renew. Energ., 2010, 35(3), 656–666.
[17] ROWE A., LI X.G., *Mathematical modeling of proton exchange membrane fuel cells*, J. Power Sources, 2011, 102(1/2), 82–96.
[18] SALEH I.M.M., CALAY R.K., ALI R., *Modelling and examining open circuit voltage for PEM fuel cell*, J. Electr. Eng., 2013, 13(3), 140–146.

inverter PQ control,
PowerSys microgrid model,
microgird control

Szymon CYGAN*
Mirosław ŁUKOWICZ*

PQ CONTROL OF PHOTOVOLTAIC POWER STATION IN MICROGRID OPERATION

The numerical modelling of the photovoltaic module and the solar inverter interconnected with the microgrid has been carried out with the use of PowerSys in Matlab/Simulink. Algorithms of P, Q controllers have been proposed. The capability of the active and reactive power reference tracking has been tested for various conditions.

1. INTRODUCTION

The contribution of distributed generation in the power system is still rising. Solar power plants become more popular each year and their presence sets new challenges for power systems. Electrical low and medium voltage grids are of radial topology and no power flow from the low to medium voltage level was anticipated in their design. New distributed generation needs the control mode allowing for cooperation with commercial electrical grid. As PV solar panels are DC sources they are connected to grid by inverters which, to generate power of specific parameters, need to be controlled.

Microgrid generators can basically operate in two modes, either connected to a commercial network or in islanding mode [1]. Islanding mode is not subject of this paper. In the network mode the solar inverter can be controlled in the Vf or PQ mode [2, 5]. The PQ mode ensures greater flexibility in satisfying electrical system requirements and is taken into account in this paper.

* Wrocław University of Science and Technology, Department of Electrical Power Engineering, Wybrzeże Wyspiańskiego 27, 50-370 Wrocław, Poland, e-mail: Szymon.Cygan@pwr.edu.pl; miroslaw.lukowicz@pwr.edu.pl

The complexity of photovoltaic cell V-I characteristics call for using special control algorithms in the PQ mode. Output power of photovoltaic cell depends on two dominant quantities namely the light illuminance and the environment temperature. Photovoltaic model described in [4, 6] is proposed as a circuit consisting of a diode, two resistances, and direct current source linearly dependent on the light density. The relation between output voltage and current presented as V-I characteristic is specific for each cell type. It is a monotonically decreasing function, however, almost constant for low voltages. It means that forced increase of one quantity causes decrease of the second. Maximal power point (MPP) is a point on V-I characteristics at which the system generates maximum power [7]. When MPP cannot be achieved by any reason the property of a monotonic decrease may lead to instability.

The PQ controllers design for inverters operating with photovoltaic modules is a compromise between requirements set by the power system state, the maximal power point tracking, the power system stability provision and an acceptable settling time. Solutions proposed in this paper were tested on the numerical model of a microgrid with local loads which well corresponds to real microgrids.

2. INVERTER CONTROL

The inverter is a device that converts DC voltage into AC voltage with specified parameters. In can be modeled as a function f: $R^3 \to C[\mathbb{R}]$.

$$f(U, U_m, \phi) = U \sin(2\pi f t + \phi) \tag{1}$$

where U is the output voltage magnitude, ϕ is the voltage phase, f is the nominal frequency.

Voltage magnitude U cannot exceed voltage provided by photovoltaic cells, so that $U \leq U_m$. The voltage magnitude and phase (U, ϕ) influence the active and reactive power generation. The PQ control consists in setting the active and reactive power reference values and modulating the phase and magnitude of the inverter output voltage to keep the generated power as close to the preset values as possible.

The active and reactive power flow in a power system depends on parameters of powers system quantities and system topology. Controllers investigated in this research were constructed in such a way that voltage phase ϕ was dependent only on the active power generation demand. The output voltage magnitude U depended only on the reactive power flow Q. Assumption that neither ϕ is influenced by reactive power nor U is influenced by the active power allowed to simplify the mathematical model of the inverter. However, this type of controllers may be unable to keep stability in some critical conditions. The diagram of the control system of the inverter is shown in Fig. 1.

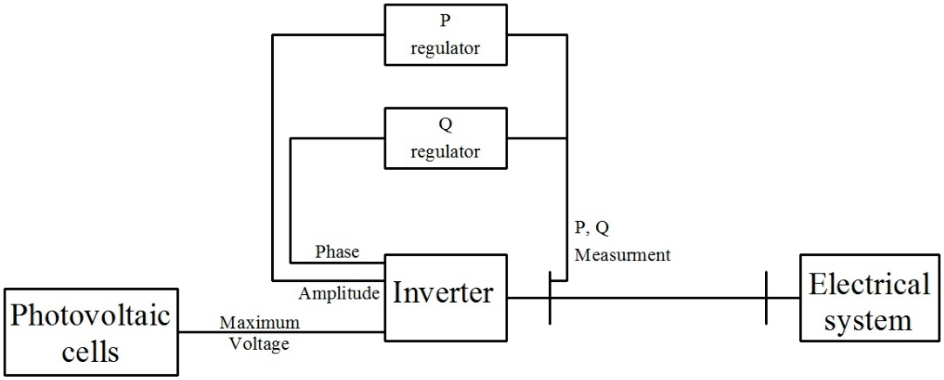

Fig. 1. Model of inverter with PQ controllers

PQ controllers are integrating elements modelled as follows

$$\frac{\partial \phi(t)}{\partial t} = \mathcal{L}^{-1}\left(\frac{a}{s+b} \mathcal{L}(P(t) - P_{\mathrm{Ref}}(t)) \right) \tag{2a}$$

$$\frac{\partial U(t)}{\partial t} = \mathcal{L}^{-1}\left(\frac{a}{s+d} \mathcal{L}(F_m(Q(t) - Q_{\mathrm{Ref}}(t))) \right) \tag{2b}$$

where $\mathcal{L}^{-1}$ is the inverse Laplace transform, F_m is a saturation function of the upper and lower limit of m and $-m$, respectively. Phase and amplitude change rates are also limited to prevent stability loosing during power flow fluctuations

$$-\phi_d \le \frac{\partial \phi(t)}{\partial t} \le \phi_d \tag{3a}$$

$$-U_d \le \frac{\partial U(t)}{\partial t} \le U_d \tag{3b}$$

Constants a, b, c, d, ϕ_d, U_d were obtained empirically to fulfill the compromise between stability loosing and a settling time.

3. MODEL DESCRIPTION

The diagram of the modeled network is shown in Fig. 2. Its arrangement allows the study of the photovoltaic module operation to be carried out under various network configuration at different loads.

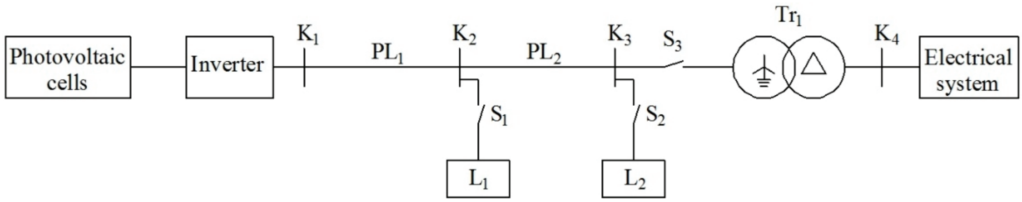

Fig. 2. Diagram of modeled section of power network

The photovoltaic power farm is connected to the network on the low voltage level 400 V at node K_1. Loads modelling local power demand are supplied at nodes K_2 and K_3 from the overhead power line PL_1. Nodes K_2, K_3 are interconnected with cable line PL_2. Since MV grid is not the subject of the study it has been modeled as a voltage source of fixed short circuit capacity. Simulations were performed for following parameters:

– Photovoltaic 11 kW power station composed of 192 Solarex MSX60 modules grouped in 8 rows of 24 modules each.
– Cable line L_1 4 × 95 XLPE of 200 m length, the per unit length resistance and reactance of 0.32 Ω/km and 0.082 Ω/km, respectively.
– Overhead line L_1 AL 70 of 300 m length, the per unit length resistance and reactance of 0.44 Ω/km and 0.31 Ω/km, respectively.
– Electric power system of 100 MVA short circuit capacity.

4. SIMULATION RESULTS

Results presented in this section concern the transients in the photovoltaic power station which can result from switching operations, changes of reference quantity values in inverter controllers, load variations, or from changes of such quantities as temperature or the illuminance dominantly influencing generating power of the photovoltaic cell. The active power diagrams presented in Figs. 3–5 relate to single phase power divided by $\sqrt{2}$. This corresponds to 2.5 kW maximal power of one phase inverter. However, the modelling was not carried out for this exact value owing to mathematical restrictions of the model and exponential error rate of calculations performed for currents close to the maximal current of the solar cell.

4.1. REFERENCE POWER CHANGE

The PQ control performance under reference power change has been investigated in the system shown in Fig. 2 with switches S1–S3 permanently closed, so that no external limits for maximal generation existed in this configuration as excess of local power could be exported to the power system. The references of active and reactive power were functions of time as presented in Table 1.

Table 1. Active and reactive power reference values vs. time

t [s]	P_{Ref} [kW]	Q_{Ref} [kVar]
0.0–0.1	0.0	0.0
0.1–0.6	0.8	0.5
0.6–1.2	1.5	0.0
1.2–1.8	2.0	0.0
1.8–2.2	2.5	0.0

Diagrams of active and reactive power in time domain in node K_1 are shown in Fig. 3. Both controllers are activated at $t = 0.1$ s. They cannot be active from the beginning due to some model restrictions. One can observe that before the activation of the controllers, the active and reactive power flow were equal to 700 W and 1.1 kVar, respectively. This values are determined by local loads L_1, L_2 and are independent of the voltage phase. The activation of controllers initiates strong power oscillations which can be observed also at $t = 0.6$ s. These oscillations are due to the fast Q control after the step change of reactive power reference. However, application of the fast Q controller almost negated overshoot after the active power reference change in instants $t = 1.2$ s and $t = 1.8$ s. One should be conscious that the overshoots of the active power are extremely dangerous when the system works close to the maximum power of solar cells what may lead to the stability loss.

The aforementioned oscillations can be eliminated by forcing ramp active loading instead of the step change. The relevant simulation results are shown in Fig. 4 where Q reference signal Q_{Ref} is ramped from 1 kvar at 0.1 s to 0 kvar at 0.6 s. It can be observed that varying Q_{Ref} extended the settling time for the active power generated. In the first case active power oscillations vanished after 300 ms. In the second case P could not be equal to P_{Ref} until reactive power reference value became constant.

4.2. NETWORK TOPOLOGY CHANGE

Generation control studies presented in Fig. 5 allows to verify capability of the controller for keeping reference power generated after the change of the local load. Active and reactive power shown in Fig. 5 are for switch S_1 closing at $t = 1.5$ s and opening at $t = 2.5$ s. Closing S_1 increases total power demand and solar cells current. In accordance with U-I cell characteristic of solar cells output voltage decreases rapidly,

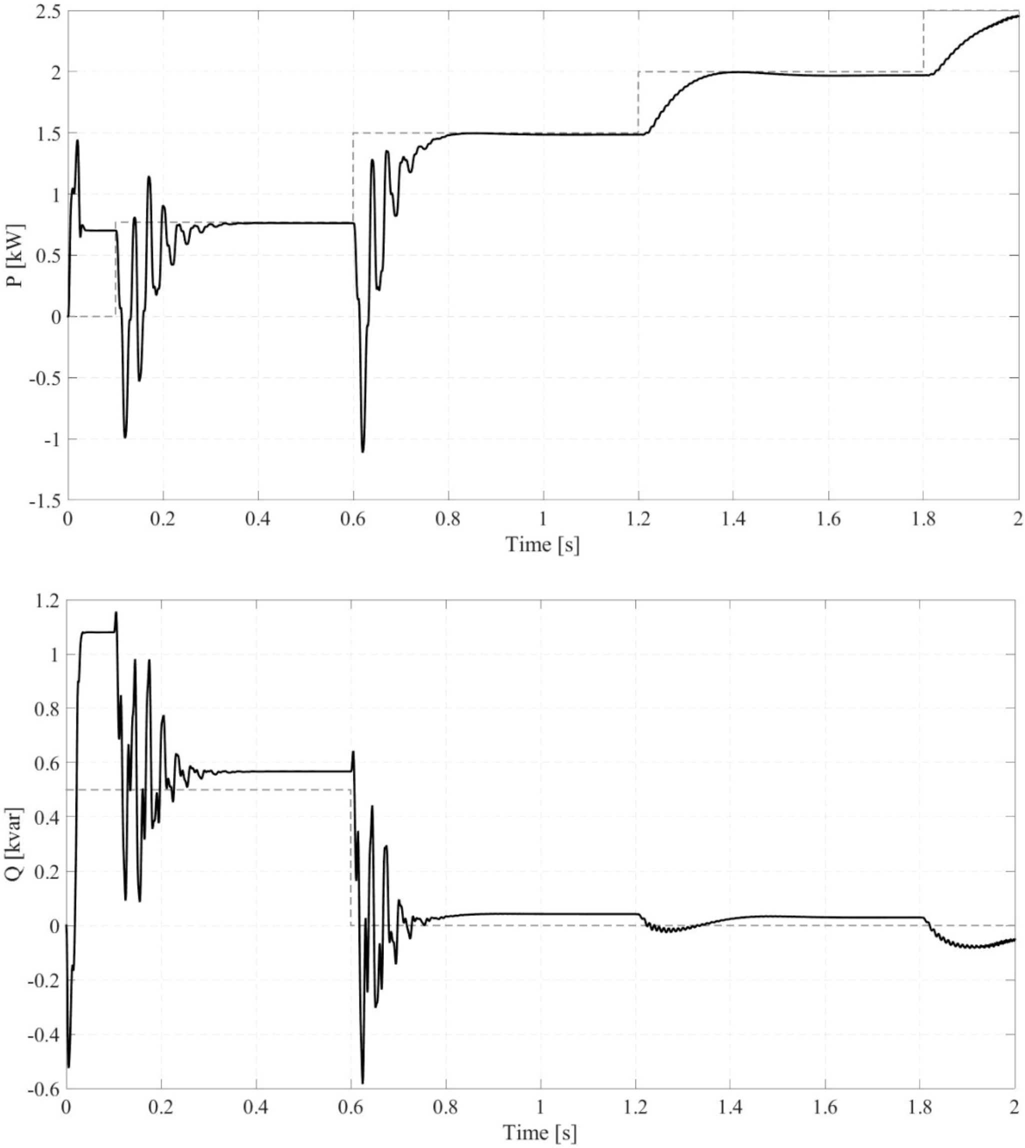

Fig. 3. Active (top) and reactive (bottom) power generation responses to step changes of the active power reference. Dashed lines are for reference signals

so that generated active power is lower. P controller changes voltage phase, reduces current and restores power flow to the reference value. Opening S_1 decreases load, and so the solar cell current. Load L_2 is R-L type therefore the switch opening results in negative Q power flow. Fast Q type control increases voltage rapidly forcing the increase of active power flow up to maximal available value, until voltage U reaches final value at t = 2.9 s. Then P controller forces active power falling below the reference value. After 2.9 s the control is performed in the same way as for switch opening.

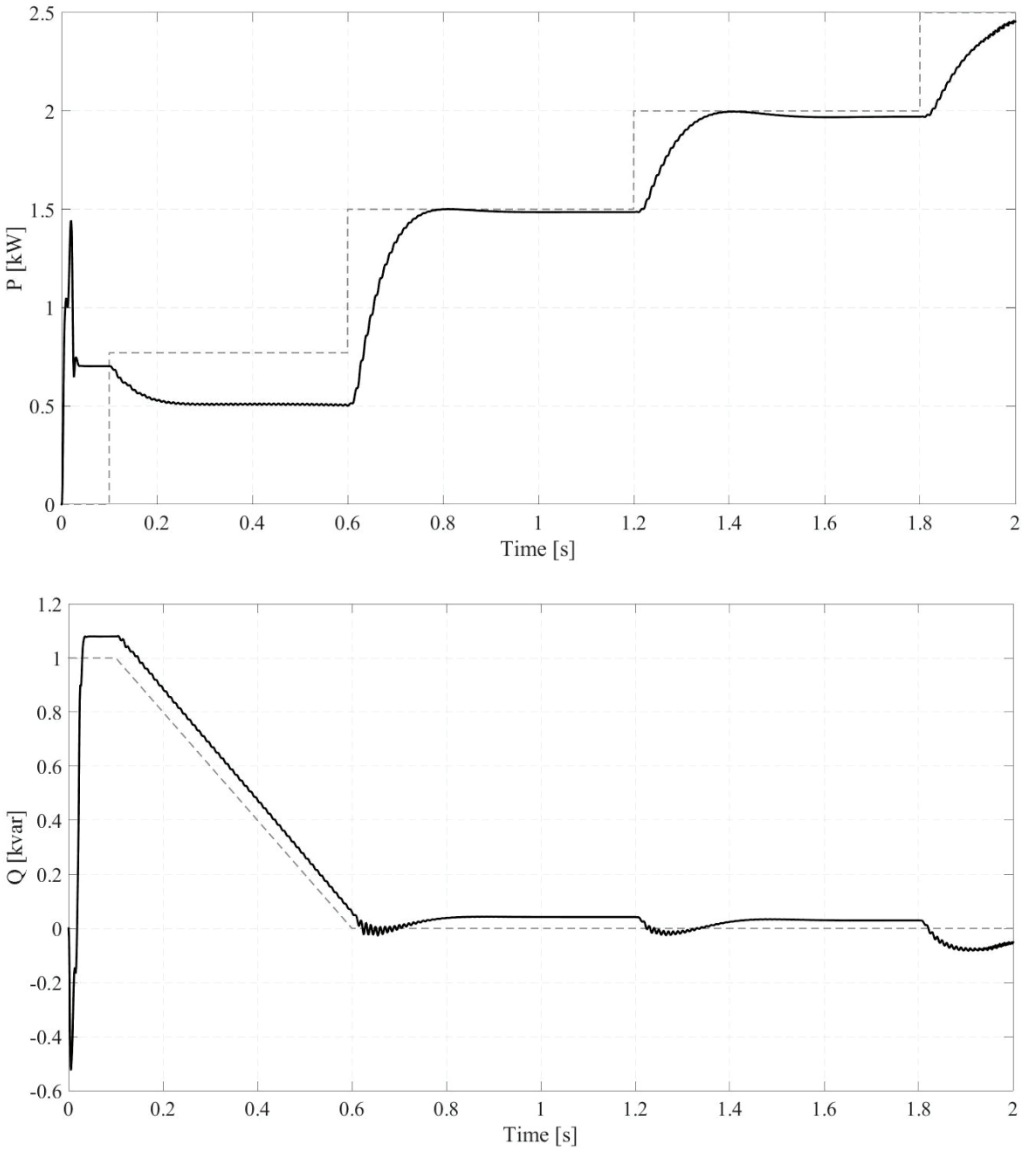

Fig. 4. Active (top) and reactive (bottom) power generation
response to ramp changing of reactive power reference.
Dashed lines are for reference signals

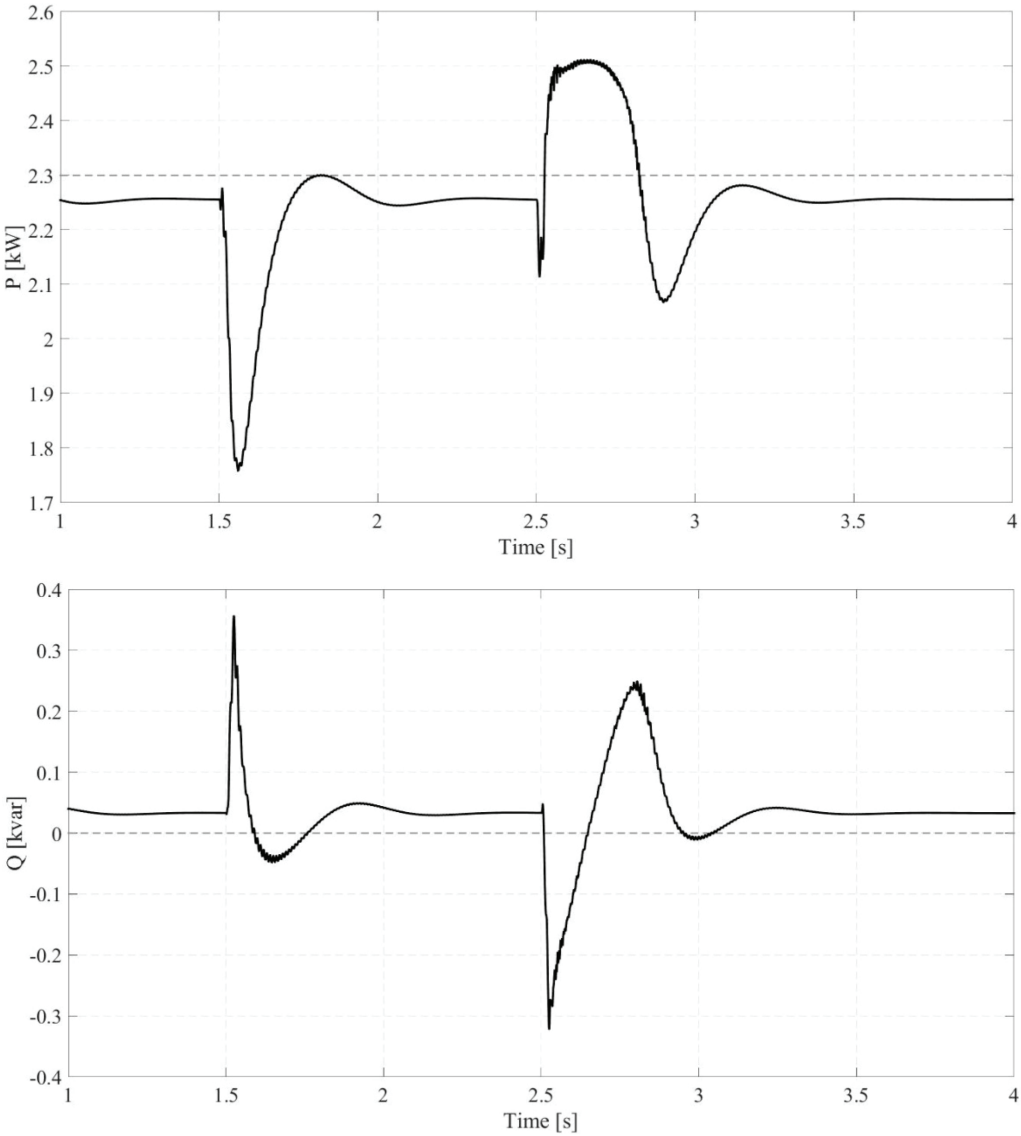

Fig. 5. Active (top) and reactive (bottom) power generation responses after S_1 on–off switching. Dashed lines are for reference signals

5. CONCLUSION

Results of PV generation control studies carried out for various grid operation modes have been presented. The goal of the research was to analyze ability of proposed P and Q controllers to stability keeping after the reference power or topology change.

It can be observed that difference between reference and real power values in steady state are dependent on the reference power value. When P_{Ref} was less than 1.5 kW then the steady state real power and the reference power were almost equal. After P_{Ref} was set to 2.4 kW, the steady state difference was more than 50 W what is due to the mathematical model specification. Photovoltaic current cannot exceed maximal cell current, even during overshoot period. Lacking 50 W was used to ensure overshoot. Excluding aforementioned problem, proposed P and Q controllers satisfy basic demands, i.e. stability is ensured with the acceptable settling time.

Depending on the user demands modified controllers can be proposed. When a settling time requirements are not so strict the ramp change of the reference signals can be applied with the change rate dependent on the required settling time. However, this modification can be related only to the reference value change mode.

REFERENCES

[1] HAJIMIRAGHA A., *Generation Control in Small Isolated Power Systems*, Master's Thesis, Royal Institute of Technology, Department of Electrical Engineering, Stockholm 2005.

[2] ADHIKARI S., LI F., *Coordinated Vf and PQ control of solar photovoltaic generators with MPPT and battery storage in micro grids*, IEEE Transactions on Smart Grid, 2014.

[3] MILOSEVIC M., ANDERSSON G., *Generation control in small isolated power systems,* Proceedings of the 37th Annual North American Power Symposium, 2005.

[4] MAHMOUD Y., EL-SAADANY E.F., *A Photovoltaic Model With Reduced Computational Time*, IEEE transactions on industrial electronics, Vol. 62, No. 6, June 2015.

[5] HAJILU N., GHAREHPETIAN G.B., HOSSEINIAN S.H., POURSISTANI M.R., *Power Control Strategy in Islanded Microgrids Based on VF and PQ Theory Using Droop Control of Inverters*, International Congress on Electric Industry Automation (ICEIA), Shiraz University, Iran, 2015.

[6] GRAMA A., DAN M., LÁZÁR E., *Photovoltaic Panel Model Using Matlab*, 39th International Spring Seminar on Electronics Technology (ISSE), Applied Electronics Department Technical University of Cluj-Napoca, Cluj-Napoca, Romania, 2016.

[7] GARG R., SINGH A., GUPTA S., *PV Cell Models and Dynamic Simulation of MPPT Trackers in MATLAB*, International Conference on Computing for Sustainable Global Development (INDIACom), Electrical Engineering Department, Delhi Technology University, Delhi, India, 2014.